Check for updates

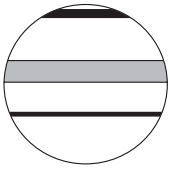

Research Paper

The Holocene
1–31
© The Author(s) 2026

Article reuse guidelines:
sagepub.com/journals-permissions
DOI: 10.1177/09596836251414044
journals.sagepub.com/home/hol

A comprehensive exposure-age dating approach to interpreting complex glacial and periglacial landscapes: The landform mosaic of Alnesdalen, a Norwegian alpine drainage basin

John A Matthews,[1] Henriette Linge,[2] Peter Wilson,[3] Richard W Mourne,[4] Paula Snook,[5] Jennifer L Hill[4] and Jesper Olsen[6]

Abstract

Our aim was to use two exposure dating techniques in combination to understand the age and development of the full complement of glacial and periglacial landforms in the Alnesdalen drainage basin, southern Norway. This required the development of a comprehensive, landscape-scale approach based on 32 ^{10}Be dates from 9 landforms and 121 Schmidt-hammer dates from 106 landforms, which identified a palimpsest landscape consisting of a mosaic of landforms of different ages. The approach enabled a spatial and temporal reconstruction of Late Glacial and Holocene glacial variations, and a deeper understanding of the periglacial, paraglacial, and paraperiglacial response of the landscape to environmental change. Results suggest that the whole of the Alnesdalen drainage basin was ice-covered by the Scandinavian Ice Sheet at the Last Glacial Maximum and that deglaciation of the valley sides and floors occurred during the Bölling-Allerød Interstadial (~14.6–12.9 ka). Dated ice-marginal moraines establish the limits of the Scandinavian Ice Sheet and of local glaciers during the Younger Dryas Stadial (~12.9–11.7 ka). Glacier extent at the maxima of the Early Holocene 'Erdalen Event' (~10.2 ka) and the Late-Holocene 'Little Ice Age' (~0.3 ka) is clarified. The periglacial response to environmental change was dominated by paraglacial processes. In the Bölling-Allerød Interstadial, large rock-slope failures were activated and talus slopes, pronival ramparts, snow-avalanche fans, large-scale patterned ground, boulder fields and boulder pavements began to form. Permafrost aggradation during the Younger Dryas may have led to the formation of a short-lived rock glacier. Large-scale patterned ground, boulder fields and boulder pavements became inactive in a seasonal-frost climate before the onset of the Early Holocene Thermal Maximum. The wide range of Holocene exposure ages from periglacial landforms with diachronous surfaces, including snow-avalanche fans, talus slopes and pronival ramparts, indicate low-levels of periglacial activity throughout a relatively benign Holocene.

Keywords

^{10}Be surface exposure dating, glacial, Late Glacial and Holocene chronology, landscape evolution, palaeoenvironmental reconstruction, paraglacial and paraperiglacial, periglacial, Schmidt-Hammer exposure-age dating

Received 3 November 2025; revised manuscript accepted 13 December 2025

Introduction

In this paper we develop an approach to understanding geomorphological landscapes based on the length of time for which land surfaces and their constituent landforms have been exposed to the atmosphere. The exposure ages of boulder and bedrock surfaces is increasingly used in the reconstruction of landscape evolution, landscape dynamics and environmental change over Holocene and Pleistocene timescales. Two complementary rock-surface dating techniques – ^{10}Be exposure dating (^{10}Be dating) and Schmidt-hammer exposure-age dating (SHD) – are applied here to the surfaces of glacial and periglacial landforms that occur in Alnesdalen, an alpine drainage basin in southern Norway (Figure 1).

^{10}Be exposure dating is a numerical-age dating technique that measures how long a rock surface has been exposed to cosmic rays at or near Earth's surface. High-energy cosmic rays interact with quartz in the rock, producing the cosmogenic nuclide ^{10}Be. The concentration of ^{10}Be increases the longer the surface is exposed. The method relies on the production rate of ^{10}Be, corrections for factors such as topographic shielding, surface erosion or snow shielding, and careful sample preparation (Balco et al., 2008). In contrast, SHD is a relatively simple calibrated-age dating

[1]Department of Geography, Swansea University, UK
[2]Department of Earth Science, University of Bergen and Bjerknes Centre for Climate Research, Norway
[3]School of Geography and Environmental Sciences, Ulster University, UK
[4]School of Architecture and Environment, University of the West of England, UK
[5]Department of Civil Engineering and Environmental Sciences, Western Norway University of Applied Sciences, Norway
[6]Aarhus AMS Centre, Department of Physics and Astronomy, Aarhus University, Denmark

Corresponding author:
John A Matthews, Department of Geography, Swansea University, Swansea SA2 8PP, Wales, UK.
Email: J.A.Matthews@Swansea.ac.uk

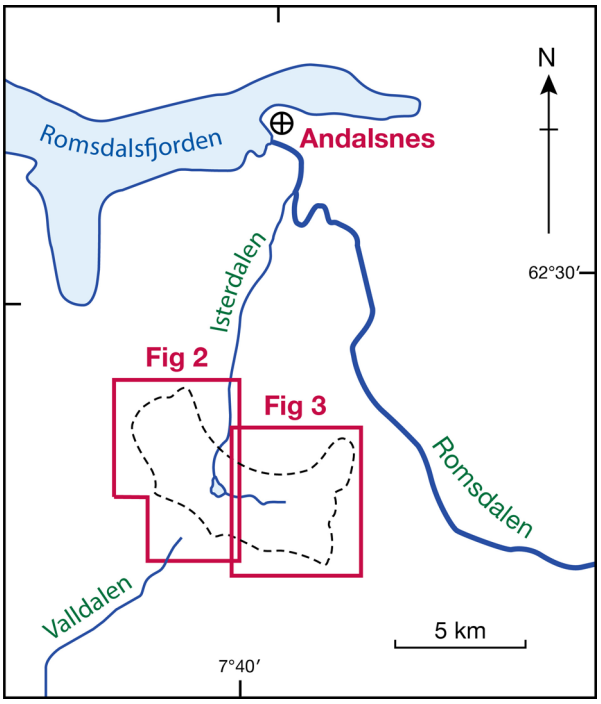

Figure 1. The Alnesdalen drainage basin (dashed black line), located about 15 km south of the coastal town of Andalsnes in the Romsdalsalpen of southern Norway. Red rectangles locate the western and eastern parts of the basin shown in detail in Figures 2 and 3, respectively. See also the inset map in Figure 2.

technique that depends on the weathering rate of rock surfaces exposed to the atmosphere. The longer the rock surface has been exposed, the weaker the rock surface and the lower the rebound value (*R*-value) recorded by a hand-held instrument as it impacts the rock surface (Matthews and Winkler, 2022).

Both techniques have been found to be particularly useful over Holocene and Late Glacial timescales and in glacial and periglacial environments where many landforms and much of the landscape are composed of exposed boulders or bedrock, and organic material suitable for radiocarbon dating is often sparse. SHD requires age-calibration, that is, establishing a numerical relationship between *R*-value and surface age based on rock surfaces of known age (Matthews and Winkler, 2022). Whereas ^{10}Be has become the exposure-age technique of choice in glacial and periglacial environments (Balco, 2011, 2020), SHD enables a larger number of dates to be obtained rapidly and cheaply. It is possible, moreover, not only to deploy both techniques in the same study but also to utilise a limited number of ^{10}Be dates in the essential procedure of SHD age-calibration (Altınay and Sarıkaya, 2025; Khashchevskaya et al., 2025; Longhi et al., 2024; Matthews et al., 2024; Santos-González et al., 2026; Tomkins et al., 2016, 2018; Wilson et al., 2019a, 2019b; Winkler, 2009).

Although both dating techniques have been applied widely to certain landform types, such as moraines, rock glaciers, rock-slope failures and alluvial fans, there have been few attempts to estimate the exposure age of the many different types of landforms that can occur within the same landscape. Examples where the dating of more than one landform type have been attempted in this way, all using SHD, include: Wilson and Matthews (2016), who dated periglacial landforms (rock-slope failures, boulder lobes, block fields, a debris cone and a talus slope), on Muckish Mountain, northwestern Ireland; Scotti et al. (2017), who dated four types of glacial and periglacial landforms (moraines, rock avalanches, rock glaciers and talus slopes) in the Val Viola, Italian Alps; Marr et al. (2019), who dated a moraine, a pronival rampart, glacially-scoured bedrock and several rock-slope failures in Opplendskedalen, southern Norway; Marr et al. (2022), who dated a blockfield, a paraglacial alluvial fan, a rock-slope failure and sorted stripes in Rondane, also in southern Norway; and Scapozza et al. (2021), who dated moraines, rock glaciers, a roche moutonée and an anthropogenic landform (Roman mule track) in the Southern Swiss Alps.

Here, for the first time, we attempt to obtain comprehensive exposure-age estimates from the full range of glacial and periglacial landforms within a single landscape unit. This involves the surfaces of erosional and depositional landforms, including moraine ridges, glacially-scoured bedrock, pronival ramparts, rock-glaciers, talus slopes, snow-avalanche fans, alluvial fans, erratic boulders, boulder pavements, patterned ground, solifluction lobes and rock-slope failures. This approach has the potential to demonstrate differences in exposure age between the different elements that comprise the contemporary landscape mosaic, requires consideration of the methodological adjustments that may be required in dating different types of landforms, and provides a basis for reconstructing the spatial and temporal complexities of landscape change.

The drainage basin or hydrological catchment can be regarded as a fundamental natural landscape unit for investigating Earth-surface processes, landform and landsystem dynamics, and the evolution of landscapes (e.g. Chorley, 1969; Makopoulou et al., 2025; Oldfield, 1977; Phillips, 2021; Toebes and Ouryvaev, 1970). However, the various landforms within any landscape, which are produced by particular processes or combinations of processes, may be active or relict and exhibit different exposure ages reflecting distinct developmental histories. Each landform, landscape element or geomorphosite (cf. Reynard, 2005; Reynard et al., 2009), therefore has the potential to make a unique contribution to understanding the landscape as a whole.

We have deliberately selected Alnesdalen as it encompasses a complex mountain landscape crossed by the limit of the Younger Dryas Ice Sheet in southern Norway (Figure 2, inset) and contains glaciers at present. As such it represents a microcosm of Norwegian glacial and periglacial landscape evolution and environmental change over at least the last ~15,000 years. Several previous studies have recognised Younger Dryas glacier limits in Alnesdalen and neighbouring areas (Carlson et al., 1983; Matthews and Wilson, 2015; Romundset et al., 2023; Wilson et al., 2020). Different parts of the Alnesdalen drainage basin were therefore expected to have been deglaciated in the Bölling-Allerød Interstadial (14.6–12.9 ka; Naughton et al., 2023a), affected by glacier growth in the Younger Dryas Stadial (12.9–11.7 ka; Naughton et al., 2023b), deglacierised shortly after the onset of the Holocene within the Greenlandian Stage (11.7–8.2 ka; Fletcher et al., 2024), and affected by neoglaciation of local mountain glaciers later in the Late-Holocene (cf. Nesje and Matthews, 2024). As well as providing a chronology of the elements of the landscape mosaic, our approach therefore has the potential to provide insights into the legacy and effects of Late Glacial and Holocene environmental changes, and a basis for palaeoenvironmental reconstruction in landscapes exposed by retreating glaciers.

The specific objectives of the paper can be summarised as follows:

(1) To demonstrate and evaluate an approach to dating the landscape based on the application of two complementary exposure-age dating techniques to the full range of glacial and periglacial landforms in a single landscape unit;

(2) To reconstruct, in as much detail as possible, both the pattern and timing of Late Glacial and Holocene glacier variations from the exposure ages of depositional and erosional glacial landforms present in the Alnesdalen catchment;
(3) To identify consistent patterns in the exposure ages of the different types of periglacial landforms that occur in environments characterised by permafrost and/or seasonal frost; and
(4) To infer the responses of the different elements of the landscape mosaic to the climatic and other environmental changes of the Late Glacial and Holocene.

Background to the Alnesdalen study area

Alnesdalen catchment occurs within the spectacular mountain landscape of the Romsdalsalpane, Møre og Romsdal, southern Norway (Figures 2 and 3). Draining towards the north, it occupies the upper part of the larger Isterdalen catchment, and lies wholly above the tree line in the alpine zone with an altitudinal range of ~700–1800 m above sea level (a.s.l.). Nearly flat valley floors contrast with steep valley sides and high-mountain ridges that have experienced multiple glacial cycles during the Quaternary.

Major features of the western part of the catchment (Figure 2) include the steep, eastern slopes of Finnan (1786 m a.s.l.) and neighbouring mountain peaks and ridges (Figure 4a), the broad valley floor of lower Alnesdalen (Figure 4b) containing Alnesvatnet (744 m a.s.l.), and the short hanging valley containing Bispevatnet (1000 m a.s.l). The eastern part of the catchment (Figure 3), which lies entirely within the Reinheimen National Park, contains the middle and upper valley of Alnesdalen (Figure 5a), which extends from Alnesvatnet to Børtjønna (1069 m a.s.l.), and a hanging valley unnamed on topographic maps (termed Skarfjelldalen by us), the floor of which lies ~1150–1250 m a.s.l. (Figure 5b). The mountain ridges surrounding these valleys commonly rise above 1500 m a.s.l. and the highest summit of Breitinden reaches 1797 m a.s.l.

Two substantial east-facing cirque glaciers are present today on Finnan (Figures 2 and 4a) with areas of 0.71 and 0.58 km^2, and minimum elevations of 1124 and 1199 m a.s.l., respectively (Andreassen and Winsvold, 2012). Aerial photographs taken over recent decades show that neighbouring smaller ice bodies on Finnan have progressively melted away (https://www.norgeibilder.no). Two very small ice bodies (glacierets) also occur on the north-facing slope of Skarfjellet near the eastern end of Skarfjelldalen (Figures 3 and 5b). The larger of these has an area of 0.04 km^2 and a minimum elevation of 1401 m a.s.l. (Andreassen and Winsvold, 2012).

Geologically, the region forms part of the Precambrian crystalline basement of the Scandinavian Caledonides (Roberts, 2003). The catchment bedrock is predominantly quartzdioritic to granitic gneiss with some banded (migmatitic), sillimanitic and augen gneiss (Tveten et al., 1998). The present-day climate of Alnesdalen is relatively mild due to the proximity of the Atlantic Ocean. At an altitude of 863 m a.s.l., mean annual air temperature is 0.8°C with mean monthly air temperatures ranging from −6.5°C to 9.8°C for February and July, respectively (Table 1). Mean annual precipitation of 1152 mm is well distributed throughout the year with an autumn and early-winter maximum. Average snow depth is ~0.5 m with up to 1.5 m in spring and two snow-free summer months. These data indicate a periglacial environment characterised by seasonal frost. The lower altitudinal limit of (discontinuous) mountain permafrost (MPA) lies at about 1600 m a.s.l. in the region (Etzelmüller et al., 2003; Etzelmüller and Hagen, 2005; Gisnås et al., 2017; Lilleøren et al., 2012). Permafrost has been detected at about 1700 m a.s.l. at Breitinden but not at Børa (1000 m a.s.l.) a much lower summit just east of the Alnesdalen basin (Dalsegg and Tønneson, 2004). Although permafrost is therefore generally absent today from all but the highest peaks, sporadic permafrost may occur above 1300–1400 m a.s.l. in steep north-facing rock slopes (cf. Magnin et al., 2019).

For much of the time during the Last Glaciation and at the Last Glacial Maximum when the Scandinavian Ice Sheet extended onto the Continental Shelf, much of the Alnesdalen catchment, at least the highest peaks and upper slopes, seems to have been covered in a cold-based ice sheet (Hughes et al., 2016; Kleman et al., 2008; Kleman and Hättestrand, 1999; Sejrup and Hjelstuen, 2022; Stroeven et al., 2016). Mapped glacial striae (Carlson et al., 1983) indicate orientations towards Isterdalen, that is, towards the north, northeast, and northwest, consistent with the orientations of the valleys. Complete deglaciation probably occurred during the Bölling-Allerød Interstadial (14.6–12.9 ka) before renewed glacierization of parts of the catchment during the Younger Dryas Stadial (12.9–11.7 ka) and rapid final deglaciation in the Early Holocene (Briner et al., 2014a, 2023; Mangerud et al., 2023; Nesje, 2009; Romundset et al., 2023; Stroeven et al., 2016). The climatic shifts that led to these major glacier variations would also have produced changes in the thermal regime of the glaciers and the nature of the periglacial environment beyond their limits, such as the extent of permafrost aggradation and degradation (Blikra and Nemec, 1998; Lilleøren et al., 2012; Matthews and Nesje, 2022).

Methods

Landform classification and mapping

Glacial and periglacial landforms were classified into 15 distinct landform types based mainly on established morphological criteria but also taking into account landform composition and position in the landscape. Maps were prepared based on aerial photographic images taken between 2012 and 2019 (https://www.norgeibilder.no/) ground truthed by field inspection and interpretation.

Glacial landforms. These included: (1) terminal and lateral moraine ridges; (2) glacially-transported boulders perched on bedrock outcrops (boulders on bedrock); (3) glacially-transported boulders embedded in till surfaces (boulders on till); and (4) glacially-scoured bedrock. *Moraines* were recognised as ice-marginal by their arcuate to linear ridge form with distinct proximal and distal slopes. They are located on valley floors or valley sides (deposited by valley glaciers), or in close proximity to extant glaciers, or in locations inferred to have been occupied by former cirque glaciers. Selected examples are shown in Figure 6a to d. With the exception of moraines associated with glacierets and very small cirque glaciers, they are composed of diamicton (till) with embedded sub-angular to subrounded boulders that result from erosion and abrasion in the basal transport zone of glaciers (cf. Boulton, 1978; Matthews, 1987). Glacially-transported *boulders on bedrock* and similar *boulders on till* were distinguished by their sub-angular to subrounded shapes combined with their association with either glacially-scoured bedrock or diamicton. *Glacially-scoured bedrock* was identified by its generally smooth, abraded surface and gently sloping profile (many sites represent the stoss side of roches moutonnées) sometimes with grooves (p-forms) and/or striations.

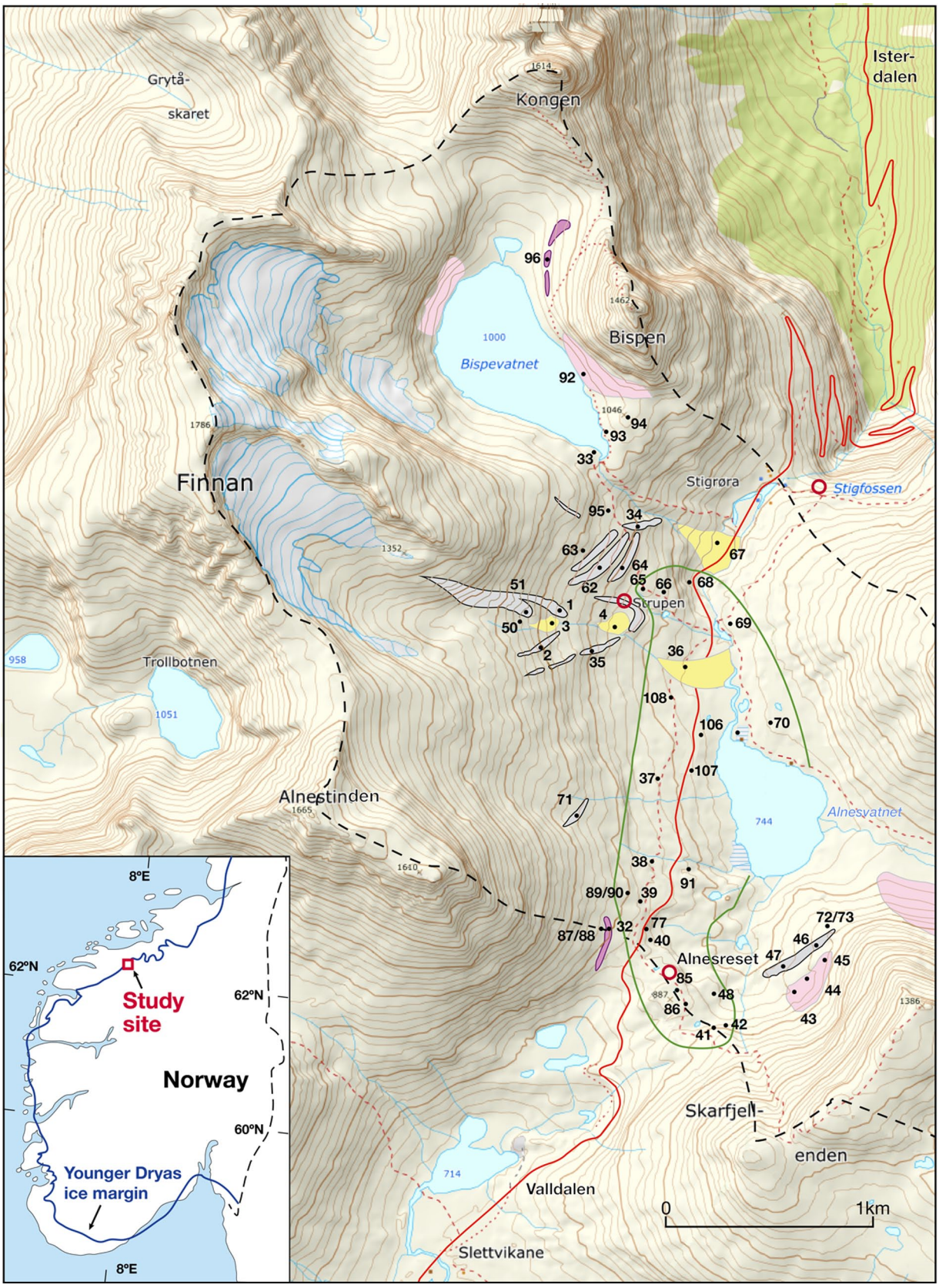

Figure 2. Western part of Alnesdalen drainage basin showing major landform types and locations of sites of ^{10}Be and Schmidt-hammer exposure-age dating. The inset map of southern Norway shows the location of the study area, which straddles the margin of the Younger Dryas ice sheet. See eastern part of the catchment (Figure 2) for key. Base map from https://www.norgeskart.no/ with 20 m contour interval.

Periglacial landforms. Throughout this paper the term 'periglacial' refers to the landforms of non-glacial cold environments (Ballantyne, 2018). These include not only the landforms associated with freezing of the ground (permafrost and seasonal frost) but also landforms shaped by more widely occurring azonal processes. Included in this study are (5) pronival ramparts; (6) a possible rock glacier; (7) alluvial fans; (8) talus slopes; (9) snow-avalanche fans; (10) snow-avalanche-scoured bedrock; (11)

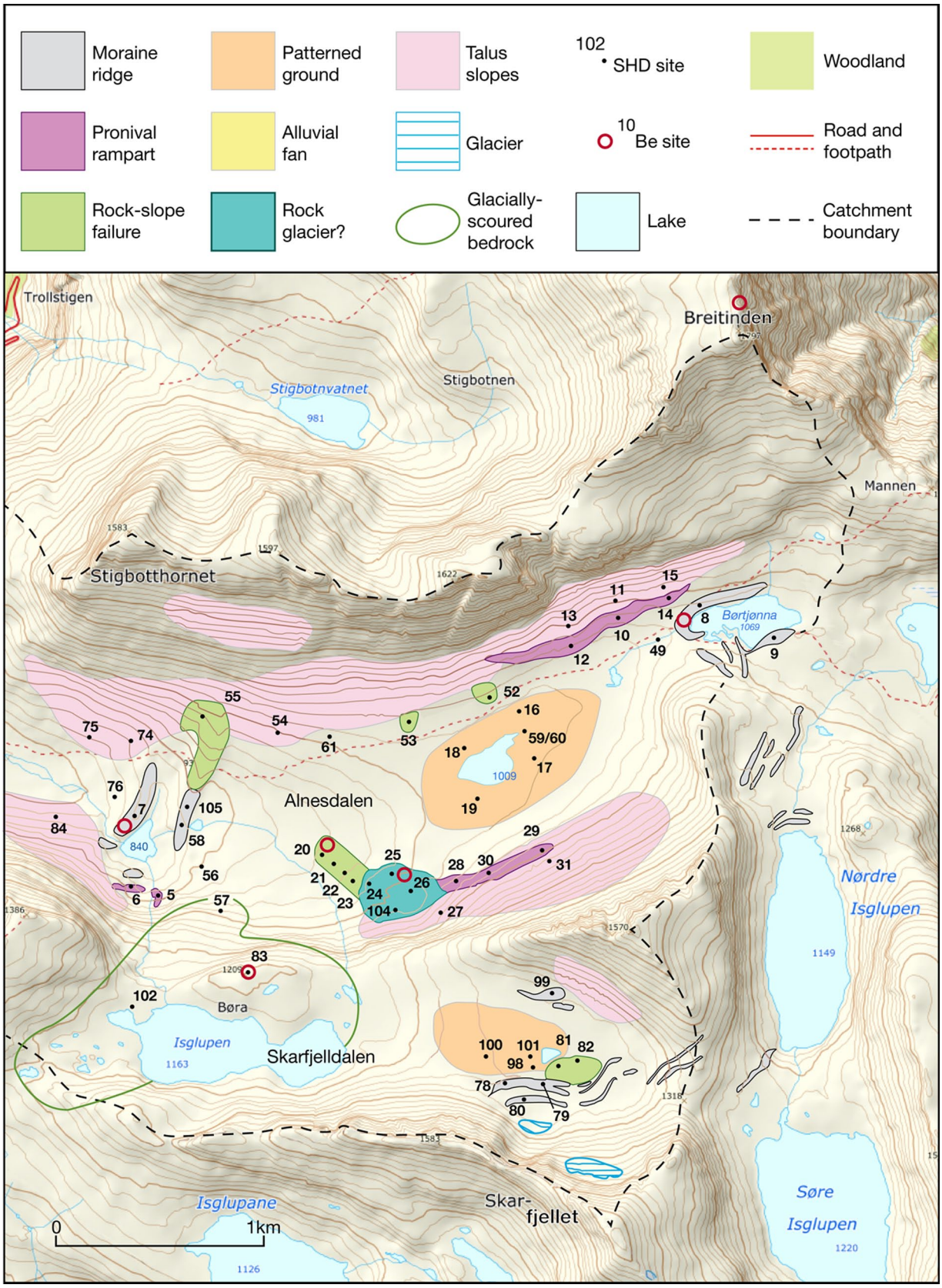

Figure 3. Eastern part of Alnesdalen drainage basin showing major landform types and locations of sites of ^{10}Be and Schmidt-hammer exposure-age dating. Note that only the main areas of patterned ground and glacially-scoured bedrock are indicated. Base map from https://www.norgeskart.no/ with 20 m contour interval.

rock-slope failures; (12) patterned ground; (13) solifluction lobes; (14) boulder fields and (15) boulder pavements. Selected examples from Alnesdalen are shown in Figures 7a to d and 8a to d. *Pronival ramparts* were distinguished from moraines by their location close to cliffs and/or talus on lower valley-side slopes with insufficient space for a glacier, strongly asymmetrical cross-profiles (long distal slope and very short proximal slope with debris infill behind the ridge) and angular to very angular boulders often with openwork composition (cf. Hedding and Sumner, 2013; Shakesby, 1997). A possible *rock glacier* was singled out

by its steep front, multiple arcuate ridges (possible flow structures) and indications of former ice content in the form of melt-out pits and furrows. However, the evidence for a rock glacier origin is inconclusive (see the detailed discussion in Wilson et al., 2020). *Alluvial fans* were identified as low-angle fans with braided stream channels, the rounded to well-rounded boulders characteristic of fluvial transport, and locations associated with extant or former glaciofluvial meltwater streams.

Several colluvial landform types occur near the foot of steep valley sides. *Talus slopes*, which occur beneath bedrock cliffs, are accumulations of angular to very angular boulders lying close to the angle of repose of loose particulate material. *Snow-avalanche fans* may resemble talus slopes but have a strongly developed, concave toe-slope caused by avalanche runout. Extremely angular rock shards caused by the impact of transported rockfall material are also characteristic of energetic snow avalanches and are often perched on larger boulders, while erosive avalanche tracks are often present up-slope. *Snow-avalanche-scoured bedrock* was identified where abraded areas on otherwise well-weathered bedrock surfaces occur downslope of avalanche tracks. *Rock-slope failure* deposits of variable size were recognised as irregular to lobate or tongue-shaped accumulations of rock debris extending outwards from the foot of cliffs. In addition, up-slope scars/failure niches on the cliffs usually confirmed a rock-slope failure origin.

The remaining periglacial landforms that we recognised are formed by frost-related processes (e.g. frost sorting and

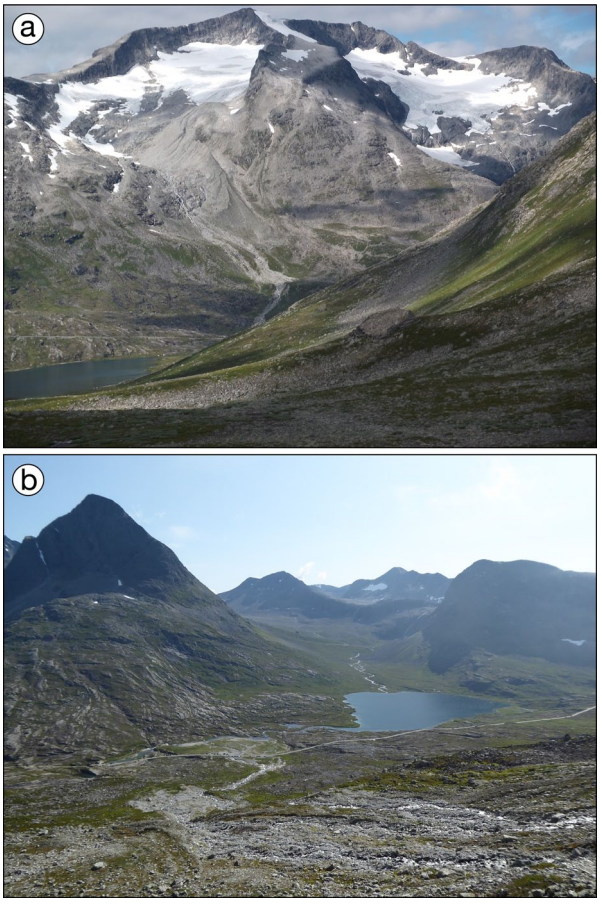

Figure 4. (a) The east-facing slope of Finnan and the southern and northern Finnan cirque glaciers viewed from upper Alnesdalen. Note moraine ridges in the middle distance, and the Alnesstein rock-slope failure in the foreground. (b) Lower Alnesdalen from the east-facing slope of Finnan. Note Alnesvatnet, extensive glacially-scoured bedrock on the valley floor, and the glaciofluvial meltwater stream from the southern Finnan glacier in the foreground.

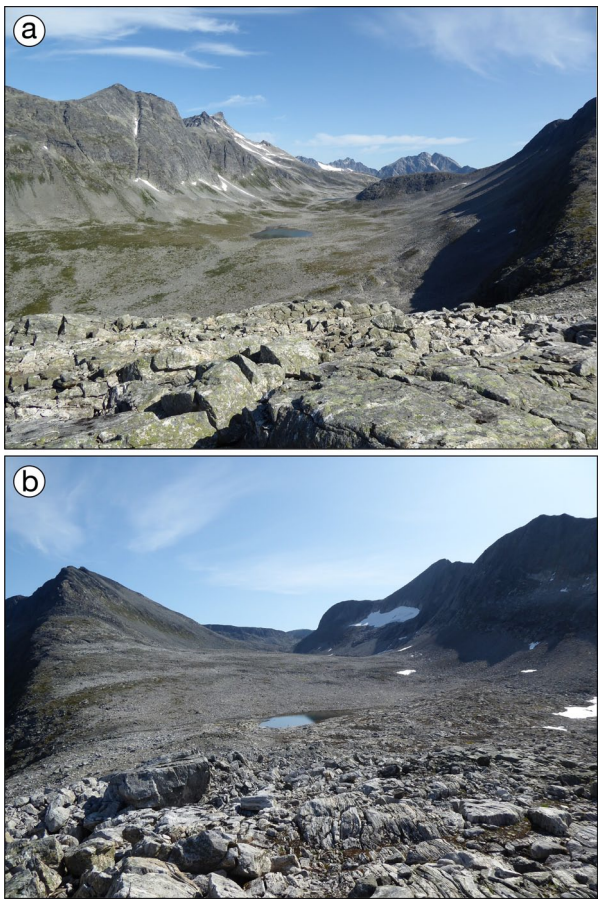

Figure 5. (a) Upper Alnesdalen, viewed from near the western end of Skarfjelldalen. Note extensive colluvial deposits (including talus slopes, pronival ramparts, snow-avalanche fans and rock-slope failures) on the lower valley-sides, and weathered glacially-scoured bedrock in the foreground. Extensive areas of patterned ground are located on the valley floor around the shallow lake (centre). (b) View up Skarfjelldalen looking east from near its western end. Note the highly weathered glacially-scoured bedrock in the foreground, the boulder field in the middle distance and the glacieret on the north-facing slope in the background.

Table 1. Mean annual and monthly climatic data (AD 1958–2017) for Alnesdalen (863 m a.s.l.).

Jan	Feb	Mar	Apr	May	Jun	Jul	Aug	Sep	Oct	Nov	Dec	Annual
Air temperature (°C)												
–6.3	–6.5	–4.7	–1.4	3.7	7.5	9.8	9.3	5.6	1.5	–3.0	–5.5	0.8
Precipitation (mm)												
109	95	93	67	53	72	82	95	120	118	116	132	1152
Snow depth (mm)												
970	1210	1410	1390	750	100	0	0	10	70	300	650	570

Source: http://www.senorge.no/.

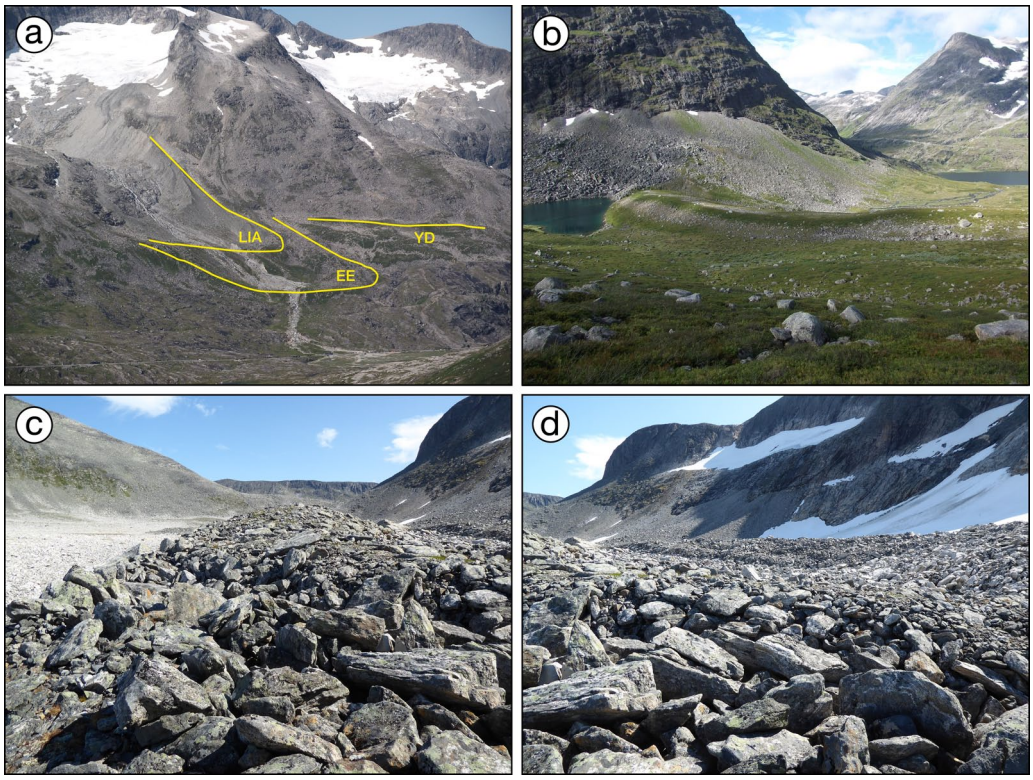

Figure 6. Selected moraines dated in this study. (a) Three generations of moraine ridges on the east-facing valley side of lower Alnesdalen beneath Finnan. Yellow lines indicate maximum glacial limits (YD: younger Dryas; EE: Erdalen event; LIA: 'Little Ice Age'). (b) Younger Dryas terminal moraine ridge crossing the floor of mid-Alnesdalen (site 7, West Alnesdalen) deposited by ice flowing up-valley from the right. Note the moraine-dammed lake to the left. (c) Younger Dryas moraine ridge (site 78) in Skarfjelldalen. (d) Late-Holocene ('Little Ice Age') moraine ridge (site 80) from the older moraine shown in (c). Note the glacierets on the north-facing slope of Skarfjellet.

gelifluction) on valley floors. These features are all associated with till deposits on valley floors in upper Alnesdalen and Skarfjelldalen. Extensive areas of large-scale, sorted *patterned ground* with circular centres of fine sediment surrounded by boulder-filled gutters were identified on the flattest parts of the valley floors above about 1000 m. *Boulder fields*, characterised by undifferentiated areas of boulders with no surface evidence of fines or sorting, and stone-banked *solifluction lobes* with distinctive risers and treads, which occur where the gradient is slightly steeper (more than a few degrees) were less common. Finally, a few areas of *boulder pavements*, defined as near-horizontal surfaces comprised of interlocking, flat-lying boulders were located in shallow river beds and along lake shorelines.

^{10}Be exposure dating

Field techniques. Using a hammer and chisel, 25 new rock samples from 7 sites were collected from the top surfaces of boulders and bedrock outcrops. A further six previously published samples from two sites (Wilson et al., 2019b, 2020) are included in this study. Sample sites, shown on Figures 2 and 3, were located in relation to landforms of strategic importance for understanding both glacial and periglacial landscape history. Sites were selected to provide critical evidence of the timing of deglaciation, Late Glacial and Holocene glacier variations, and the activation and stabilisation of periglacial landforms.

Samples of thickness 1.0–5.0 cm were taken preferentially from large (long axis 60–500 cm), stable boulders and upstanding bedrock outcrops of suitable lithology. Sampled surfaces were composed of banded gneiss, granitic gneiss, augen gneiss, sillimanite gneiss, diorite gneiss, biotite gneiss, or protruding veins, knobs or lenses of quartz. Sample locations and elevations were recorded by a Garmin Montana 600, hand-held GPS. Elevations were later checked against a digital terrain model (DTM, https://hoydedata.no/LaserInnsyn2/; NDH Rauma Sør-Norddal øst 2pkt, 0.5 m resolution, ±20 cm vertical precision).). Topographic shielding of each sample was based on clinometer readings to skyline at 20° azimuth intervals, or as required by the surrounding topography (see Dunne et al., 1999). Subsequently, topographic shielding values (including self-shielding) were calculated using the 'Calculate topographic shielding' tool in the online exposure-age calculator (Balco et al., 2008).

Site and sample descriptions. Three sites (10 boulder samples) were located on large terminal moraine ridges with the expectation that their exposure ages would provide the timing of landform stabilisation shortly following attainment of the maximum extent of glacial advances or re-advances. The West Alnesdalen moraine (Wilson et al., 2019b) is the ice-proximal (down-valley) of two ridges on the valley floor of Alnesdalen (site 7, Figures 3 and 6b). The East Alnesdalen (Børtjønna) moraine is the ice-distal (down-valley) ridge of the moraine complex surrounding Børtjønna and extending outside the Alnesdalen catchment (site 8, Figure 3). The Finnan moraine, which is located in front of one of the present-day cirque glaciers on Finnan, lies mid-way between the outermost 'Little Ice Age' moraine and the valley floor (between sites 4 and 65, Figures 2 and 6a).

Four sites (14 samples) were located within areas of bedrock where both bedrock and boulder surfaces were sampled. These samples were expected to provide minimum age estimates of when glaciers last occupied these sites. The first of these sites is located within the glacially-scoured bedrock area close to the lip of the hanging valley of Skarfjelldalen (site 83, Figure 3). The second is in the col of Alnesreset near the southern end of the

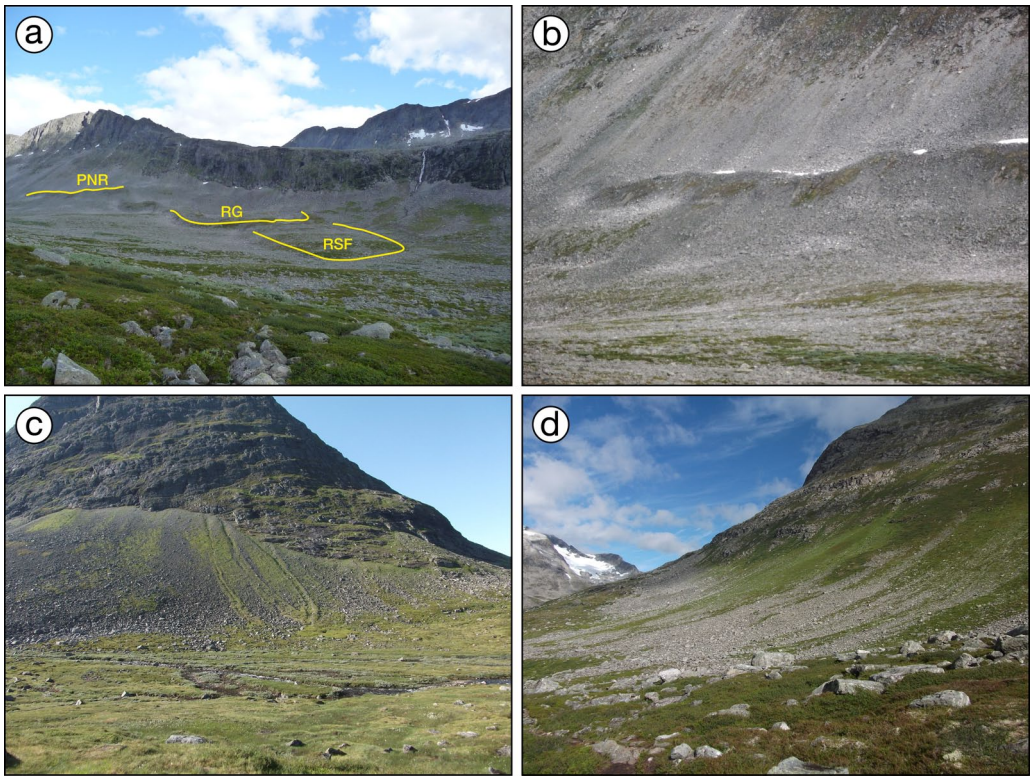

Figure 7. Selected periglacial landforms dated in this study. (a) Landform complex on the north-facing valley side of upper Alnesdalen. Yellow lines indicate a linear pronival rampart (PR; sites 28–30), the possible talus-foot rock glacier (RG; sites 24–26), and a tongue shaped rock-slope failure (RSF; sites 20–23). (b) Close-up of the pronival rampart (sites 29–30; also shown in (a). (c) Talus slope on the north-facing valley side of mid Alnesdalen (site 84). Note evidence of recent reworking by debris flows. (d) Snow-avalanche fan on the south-facing valley side of mid Alnesdalen (site 75) showing strong down-slope curvature of the distal fan surface.

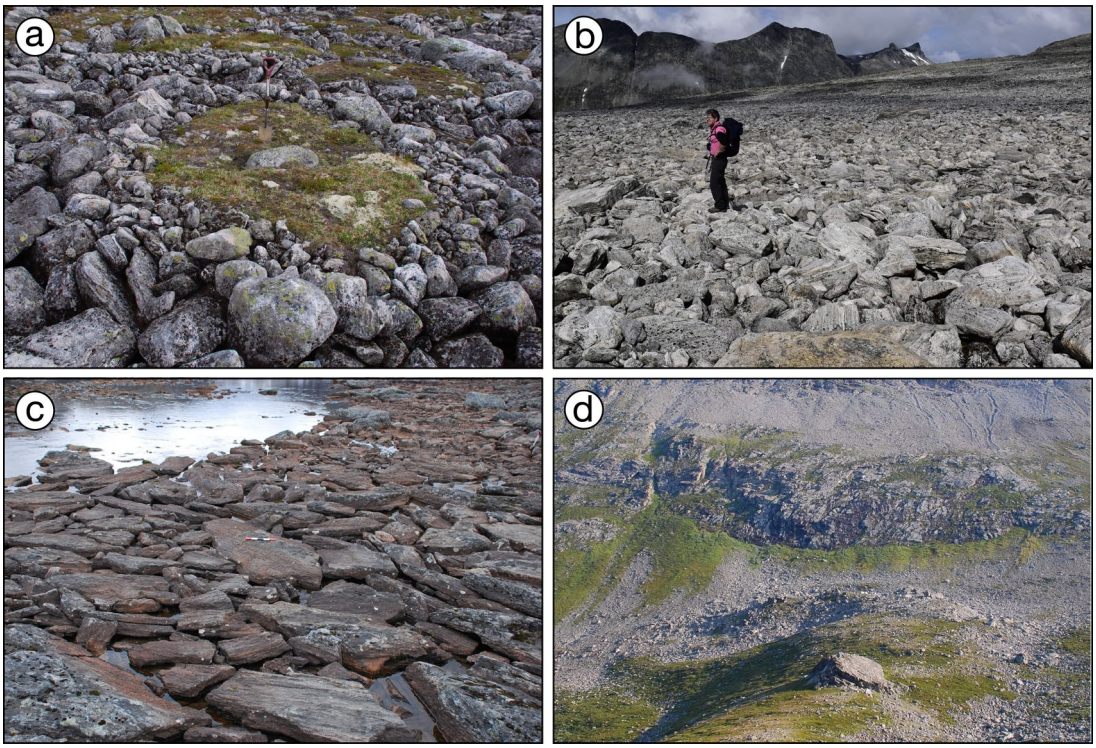

Figure 8. Further selected periglacial landforms dated in this study. (a) Patterned ground (sorted circle) in upper Alnesdalen (site 16). Note sub-angular to subrounded boulders and spade for scale. (b) Boulder field in Skarfjelldalen (site 101) with no evidence of patterned ground at the site. (c) Boulder pavement in upper Alnesdalen (site 59) showing characteristic flat-lying boulders. (d) Rock-slope failure on the south-facing valley side of mid Alnesdalen (site 55). Note the Alnesstein in the foreground at the lower end of the deposit.

extensive area of glacially-scoured bedrock in lower Alnesdalen (site 85, Figure 2). The third bedrock site (not glacially scoured) is at the summit of Breitinden, the highest point in the catchment (Figure 3). The final site of this type involved a single sample (Trollstigen viewpoint, near Stiggfosen, Figure 2) taken from a boulder lying on glacially-scoured bedrock close to the mouth of Alnesdalen catchment.

Two sites (8 samples) are associated within the boulder-dominated landform assemblage on the south side of upper Alnesdalen (Figures 3 and 7a); see Wilson et al., 2020). The first site (site 25) occurs on the upstanding outer ridge of the possible rock glacier at the centre of the complex, from which dating results have been published previously by Wilson et al. (2020). The second site (site 20) is located on the lower, outermost ridge of the tongue-shaped, rock-slope failure component of the complex.

Full ^{10}Be sample descriptions, including photographs of each site are included in Supplemental Figures and Supplemental Table S1.

Laboratory methods and age calculations. Sample processing was carried out in the Preparation Facility for Cosmogenic Nuclides at the University of Bergen and beryllium isotope ratios were measured at the Aarhus AMS Centre, Aarhus University. Full details of the laboratory methods, protocol and data are provided in Supplemental Tables S2 and S3. Details of the ^{10}Be production rate and scaling scheme used in the age calculations are also included as supplementary information.

Exposure ages were calculated using version 3.0.2 (updated 2024-08-26) of the on-line calculator formerly known as the CRONUS-Earth online calculator (Balco et al., 2008; https://hess.ess.washington.edu) employing the global ^{10}Be production rate calibration of Borchers et al. (2016) and the LSDn scaling scheme (Lifton et al., 2014). Our choice of the global production rate rather than the western Norway or Scandinavian production rates (which yield higher ages) was based on its greater consistency (particularly for elevations $>$700 m a.s.l.) when tested against the known Younger Dryas ages of 25 published and unpublished Norwegian marginal moraines sites (see preliminary publication in the poster presentation of Linge et al., 2025).

Resulting individual surface ages and site mean ages were calculated with internal and external uncertainties of $\pm 1\sigma$. In the text we use external uncertainties at 2σ, which is the most realistic option when comparing the ages from different sites and assessing similarities and differences between ^{10}Be and SHD ages. Site mean ages were calculated using the optional 'single landform' tool in the on-line calculator, which identifies statistical outliers and computes summary statistics. Internal uncertainties include measurement uncertainties only, whereas external uncertainties include uncertainty of the ^{10}Be production rate and the ^{10}Be decay constant. Raw ages include site-specific topographic (including surface slope) shielding but no correction for glacial isostatic land elevation changes (land uplift), temporary snow shielding or rock-surface erosion. Our preferred ages are those including all three corrections, each of which resulted in older ages than the raw ages.

Land uplift was estimated based on multiple sources: a sea-level curve constructed from an age-calibrated version of the shoreline diagram for the Sunnmøre–Sør-Trøndelag region (Svendsen and Mangerud, 1987); the observed marine limit of 125 m a.s.l. in Valldalen (Stokke, 1983); the modelled marine limit in Isterdalen (Norges geologiske undersøkelse, 2025); and a total post-Younger Dryas uplift of 100 m inferred from the isobase map of Svendsen and Mangerud (1987, modified from Sollid and Kjenstad, 1980). The inner fjord areas show a change from rapid to slow emergence around 9–8 ka with about 7% of the uplift prior to 12 ka, about 61% of the uplift between 12 and 8 ka, and 32% thereafter. This translates into the average elevations for surfaces exposed for 14, 13, 12, 11 and 10 ka having been 40, 35, 30, 24, and 19 m lower than the present-day elevations, which are similar to those obtained when using the 'correction for elevation' tool (GIA model: ICE-6G) available from the iceTEA calculator (Jones et al., 2019). As the shoreline diagram does not extend further back in time, we use the iceTEA estimate of 80 m lower mean elevation for our Breitinden site. An average elevation of 40 m lower than the present amounts to about 3.6% increase in age, whereas 24 m lower average elevation gives an increase in age of 2.2%. The correction for elevation change alone amounts to 2.7% increase in age (e.g. 316 years for a raw age of 11.7 ka) relating to the Younger Dryas/Holocene transition).

A conservative snow-shielding correction was tentatively estimated from 25% of modelled modern (AD 1958–2020) daily snow depth values for Alnesdalen (http://www.senorge.no/). This amounts to 4% (Alnesdalen), 6% (Skarfjelldalen) and 8% (Breitinden) older ages (e.g. 468 years for a raw age of 11.7 ka from Alnesdalen). Exposure ages from our gneissic surfaces were corrected for an average erosion rate (surface lowering) of 1.3 mm ka^{-1}. This rate is based on the average relief of 16 mm for 44 observed quartz veins, lenses and knobs of quartz protruding above rock surfaces to the north, east and south of Alnesvatnet. No correction was necessary for quartz surfaces. Similar average rock-surface weathering and erosion rates appear to be widely applicable to crystalline lithologies elsewhere in the Scandinavian mountains (André, 2002; Linge et al., 2020; Matthews and Owen, 2011; Nicholson, 2009). The correction for erosion alone amounts to less than 2% older ages (e.g. 152 years for a raw age of 11.7 ka).

Schmidt-hammer exposure-age dating (SHD)

Field techniques. In sampling rock surfaces for SHD, our ambition was to be as comprehensive as possible in covering the range and disposition of landforms present in the Alnesdalen basin. At least two sites from each of the 15 landform types identified during mapping were selected for measurement of Schmidt hammer impacts (*R*-values). More sites were selected in areas of the catchment of importance for reconstructing glacial history (e.g. where different generations of moraines were in evidence) and also where the landforms were most typical and/or numerous (Figures 2 and 3).

At each site we aimed to measure 200 *R*-values, 100 each in two contiguous plots, the size of which depended on the quality of the rock surfaces. Use of 200 impacts has been found previously, in relation to a wide range of gneissic rock in southern Norway, to be sufficient to reduce age-resolution to between 500 and 1000 years (Matthews and Winkler, 2022). Sub-dividing the sample into two sub-samples, enabled detection of any significant variation in *R*-values across the landform and hence was regarded as a test of the existence of a diachronous surface (i.e. a surface not of uniform exposure age and hence not formed in a single short-lived event). In those cases where significant differences were detected between the two plots, the sub-samples were treated separately in further analysis. Out of an initial 107 sites sampled in this study, 14 have been split in this way into A and B sites yielding a final total of 121 sites to be analysed separately.

Measurements were made with mechanical N-type Schmidt hammers (Proceq, 2017). These calibrated instruments were frequently tested for deterioration while in the field using a portable test anvil. For landforms composed of boulders, one impact was recorded from each of 200 boulders. For bedrock surfaces, 200 impacts were spread across a wide area of the rock surface

involving, where available, more than one closely adjacent rock outcrop. In a few cases, the specified sample sizes differed, most notably where landforms and data have been used from our previously published studies on particular landforms within the catchment (Matthews and Wilson, 2015; Wilson et al., 2020). Whether boulders or bedrock were sampled, the intention was for the measurements to include the local lithological variability in the predominantly gneissic bedrock while avoiding schistose and quartzitic lithologies, the weathering rate, compressive strength and *R*-values of which are appreciably different (Matthews et al., 2016).

Points of impact on rock surfaces were restricted in order to minimise other types of non-age related variability that potentially affect *R*-values. These include confining impacts to horizontal or sub-horizontal rock surfaces, avoiding unstable boulders, structural defects, cracks and edges, and lichen or moss cover, and carrying out measurements only when surfaces were dry (cf. Karakul, 2017, 2020; Shakesby et al., 2006; Sumner and Nel, 2002). No abrasive pre-treatment of the rock surface was carried out at points of impact prior to measurement, and no attempt was made to identify and reject anomalous readings during measurement (other than those obviously due to rock crystal crushing or instrument slippage).

Age calibration. This was carried out using the 'two-point solution' first proposed by Matthews and Owen (2010) and most recently outlined in full by Matthews and Winkler (2022). Based on 'young' and 'old' surfaces of known age (control points), the two-point solution establishes a linear relationship between mean *R*-value and exposure age. This relationship is described numerically and graphically by the calibration equation and calibration curve, respectively. Confidence intervals around each predicted age depends on the statistical uncertainties associated with both the error of the calibration equation (*Cc*), which depends on the uncertainties of the control points, and the sampling error (*Cs*) associated with the sample measurements at particular sites.

We have introduced an important modification to the calculation of *Cc*, which results in confidence intervals for age of ±1035–1835 years. These intervals are around twice the width of those obtained in previous applications of the two-point solution. The modification involves combining the mean *R*-values from several separate control surfaces to form each control point (Table 2). Each combined mean *R*-value is calculated using the weighted average sample size rather than the total sample size. For example, the control point for 'young moraine boulders and road-cut bedrock' uses a weighted average sample size of 180 rather than the total sample size of 900 individual *R*-values. The resulting broader confidence intervals for age better reflect the large variability in *R*-values between sites of the same age and hence are more realistic representations of the uncertainties than those used formerly.

For young control points we utilised data from moraine boulders, glacially-eroded bedrock, alluvial boulders and anthropogenic road-cut bedrock. Modern moraines on the glacier foreland of the South Finnan Glacier (Figure 6a) are considered to have been deposited between the well-established maximum 'Little Ice Age' extent of southern Norwegian glaciers in the mid-eighteenth century (~260 years ago), and the last moraine-building event of the 'Little Ice Age' in the AD 1930s (~80 years ago; cf. Nesje and Matthews, 2024). Although local documentary evidence is lacking, the proximity of these moraines to the present-day glacier, their fresh non-weathered appearance and the sparse vegetation cover fully support this assertion. Glacially-scoured bedrock with an exposure age of ~80 years was located closely proximal to the youngest moraine ridge. An age of 20 years was assumed for modern alluvial boulders deposited and reworked by the present glaciofluvial meltwater stream of the same glacier at downstream locations (see Figure 6a). As the current road between Valldalen and Isterdalen was constructed in AD 1936 (Tennøy and Askheim, 2025), bedrock surfaces excavated in the road cuts were assigned an exposure age of 80 years.

Our old control points utilised all the available ^{10}Be-dated surfaces from the Alnesdalen catchment. These included moraines, a rock-slope failure, the possible rock glacier and glacially-scoured bedrock sites as indicated in Table 2.

Table 2. *R*-value data from young and old control surfaces of known exposure age from within the Alnesdalen catchment. Combined values (in italics or bold) are averages for more than one site weighted according to sample size as explained in the text. Combined values in bold are those used to calculate age-calibration equations.

Control Site	Age (Years)	*N*	Mean *R*-value	S.D.	C.I. (95%)
Young moraine boulders					
Site 1	260	200	56.4	11.0	1.55
Site 2	260	200	55.5	8.14	1.14
Site 51	80	200	55.2	7.73	1.09
Combined	*200*	*200*	*55.7*	*9.41*	*1.32*
Young road-cut bedrock					
Site 68	80	200	55.2	7.07	0.99
Site 77	80	100	56.9	5.10	1.02
Combined	*80*	*150*	*55.7*	*6.50*	*1.05*
Young moraine boulders and road-cut bedrock					
Combined	**160**	**180**	**55.7**	**8.57**	**1.26**
Young alluvial boulders					
Site 3	20	100	61.8	7.10	1.41
Site 4	20	100	57.1	8.30	1.64
Site 36	20	200	57.5	8.77	1.23
Combined	*20*	*133*	*58.5*	*8.47*	*1.46*
Young glacially-scoured bedrock					
Site 50	80	200	60.2	6.70	0.94
Young glacially-scoured bedrock and alluvial boulders					
Combined	**40**	**150**	**59.1**	**7.94**	**1.29**
Old moraine boulders					
Site 7A	12,650	175	40.2	9.67	1.44
Site 7B	12,650	200	39.1	9.33	1.31
Site 8	13,110	200	38.6	8.30	1.17
Site35	10,770	200	36.0	9.32	1.31
Combined	*12,283*	*194*	*38.4*	*9.15*	*1.30*
Old rock-glacier? Boulders					
Site 24	14,450	200	37.7	8.34	1.17
Site 25	14,450	200	39.2	8.35	1.17
Site 26	14,450	200	38.0	9.24	1.29
Site 104	14,450	200	38.2	8.57	1.20
Combined	*14,450*	*200*	*38.3*	*8.63*	*1.21*
Old rock-slope failure boulders					
Site 20	12,220	200	38.9	8.13	1.14
Site 21	12,220	200	38.2	7.86	1.10
Site 22	12,220	200	38.3	8.05	1.13
Site 23	12,220	200	38.6	8.40	1.17
Combined	*12,220*	*200*	*38.5*	*8.11*	*1.13*
Old moraine, rock glacier and rock-slope failure boulders					
Combined	**12,984**	**198**	**38.4**	**8.63**	**1.21**
Old glacially-scoured bedrock					
Site 83A	14,550	100	38.7	8.06	1.60
Site 83B	14,550	100	42.8	7.90	1.57
Site 85	12,400	200	37.6	8.02	1.13
Site 86	12,400	200	38.7	8.05	1.13
Old glacially-scoured bedrock					
Combined	**13,116**	**150**	**39.0**	**8.02**	**1.30**

N: sample size; S.D: standard deviation; C.I: confidence interval.

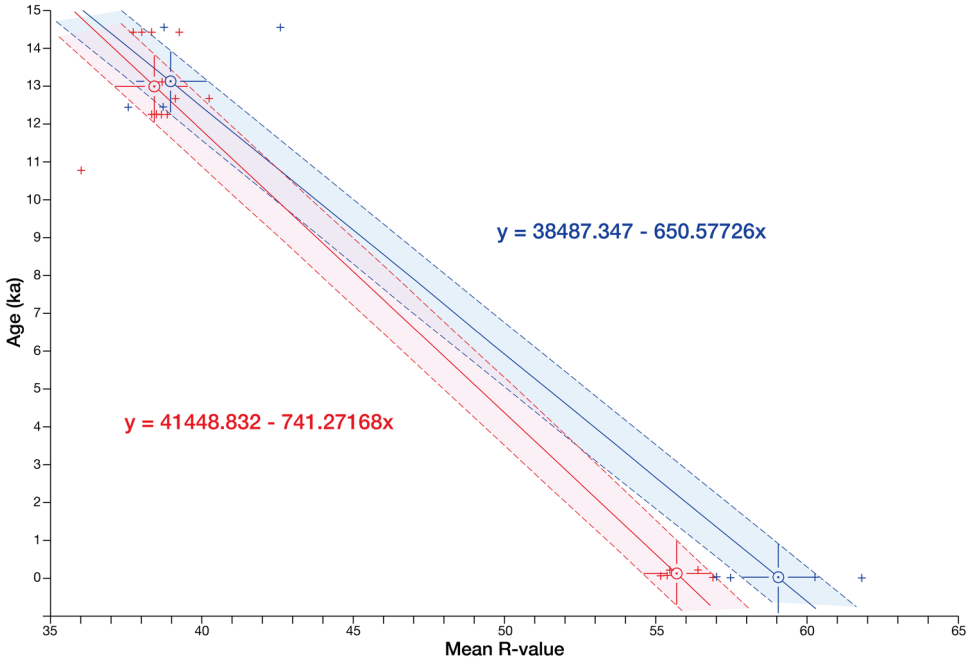

Figure 9. Relationships between mean *R*-value and surface exposure age represented as linear age-calibration curves and age-calibration equations. Mean *R*-values for individual sites (crosses) and the corresponding combined mean values for old and young control points (circles with 95% confidence intervals) are also shown. Colours distinguish between initially glacially-scoured bedrock and alluvial boulders (blue), and the initially rougher surfaces of boulders from colluvial landforms, moraine ridges and road-cut bedrock (red). See text for further explanation.

Separate calibration equations and calibration curves were calculated for two types of rock surface that yielded different mean *R*-values for surfaces of the same age. The first type of surface involved boulders from moraines and road-cut bedrock for the young control point; and moraine boulders, the rock-glacier and a rock-slope failure for the old control point. The second type of surface involved glacially-scoured bedrock and alluvial boulders for the young control point; and glacially-scoured bedrock for the old control point. Use of two age calibrations was necessitated by the distinctly higher mean *R*-values characteristic of young rock surfaces that have been strongly abraded by glacial or glaciofluvial processes. In contrast, lower *R*-values are characteristic of the rougher granular rock surfaces that are produced by frost weathering or subjected to colluvial processes in periglacial environments (cf. Matthews and Mcewen, 2013; Olsen et al., 2020). After prolonged weathering, therefore, the mean *R*-values of old surfaces of both types converge and become statistically indistinguishable, as can be seen in Figure 9.

Results

^{10}Be ages and their interpretation

^{10}Be age estimates for individual samples and sites with and without corrections, with 1σ internal and external uncertainties are presented in Table 3. Mean corrected ages are visualised in Figure 10. In the following text corrected age estimates and 2σ external uncertainties are used unless otherwise stated. Ages are reported with uncertainties rounded to one significant figure, and central values rounded accordingly.

The oldest raw ^{10}Be ages of 17.3 ± 2.3 to 116 ± 15 ka are from the bedrock samples from the summit of Breitinden. The youngest of these has a ^{26}Al/^{10}Be value of 5.8 ± 0.3 (Supplemental Table S3) indicating a complex exposure history, and hence the corrected exposure age of 20.2 ± 2.8 ka (BREI-02) is interpreted as a reliable maximum estimate of the timing of deglaciation following wastage of the Scandinavian Ice Sheet shortly after the Last Glacial Maximum. The significantly greater ages of the other samples are attributed to inherited ^{10}Be (alternative interpretations are discussed below).

The valley-floor moraine ridges from West and East Alnesdalen yielded corrected mean ages of 12.7 ± 1.6 and 13.1 ± 1.7 ka, respectively. As each of these mean ages is based on three samples that produced consistent results, they are interpreted as reliable estimates of the timing of moraine stabilisation. Although the uncertainties are large, moraine deposition clearly occurred during the Younger Dryas Stadial, which lasted for around 1200 years between ~12.9 and 11.7 ka. This conclusion is in line with previous interpretations of the age of the West Alnesdalen moraine and proposed Younger Dryas glacier limits throughout the region (Carlson et al., 1983; Matthews and Wilson, 2015; Romundset et al., 2023; Wilson et al., 2020).

Three dated samples from the Finnan moraine gave ages younger than the other ^{10}Be-dated moraines. The mean age of 10.8 ± 1.4 ka obtained from this moraine is consistent with moraine deposition by a local glacier in the Early Holocene.

Two bedrock samples from the area of glacially-scoured bedrock in Skarfjelldalen and two samples from boulders on bedrock yielded a corrected mean ^{10}Be age of 14.6 ± 1.8 ka. There is therefore little or no doubt that this site was deglaciated in the Bölling-Allerød Interstadial (14.6–12.9 ka) as the Scandinavian Ice Sheet downwasted and/or retreated from the area.

In contrast, the corrected mean age of 12.4 ± 1.5 ka from Alnesreset for the four consistent bedrock samples is appreciably younger and similar to the age of 12.6 ± 1.7 ka (TROLL-1) obtained from the single boulder lying on bedrock from the Trollstigen viewpoint at the mouth of the Alnesdalen basin. The ages of both sites suggest Younger Dryas deglacierisation but, due to the scale of the uncertainties, an earlier deglaciation age cannot be ruled out.

The remaining ^{10}Be ages, which were obtained from the periglacial boulder-dominated landform complex in upper Alnesdalen, were expected in the light of their location to yield older

Table 3. Summary of ^{10}Be surface exposure ages for each sampled surface obtained from the online exposure age calculator formerly known as the CRONUS-Earth online exposure age calculator (Balco et al., 2008; https://hess.ess.washington.edu) using the global production rate (Borchers et al., 2016) and LSDn scaling (Lifton et al., 2014).

Sample ID	Raw age (ka)	Average elevation change (m)	Uplift-corrected age (ka)	Uplift- and snow-shielding-corrected age (ka)	Uplift-, snow-shielding-, and erosion-corrected age (ka)
West Alnesdalen moraine (Wilson et al., 2019b)					
ALN 1701	11.18 ± 0.59 (0.89)	30	11.50 ± 0.61 (0.91)	11.89 ± 0.63 (0.94)	12.05 ± 0.64 (0.97)
ALN 1702	11.91 ± 0.49 (0.86)	30	12.23 ± 0.50 (0.88)	12.65 ± 0.52 (0.91)	12.83 ± 0.54 (0.94)
ALN 1703	11.88 ± 0.40 (0.81)	30	12.20 ± 0.41 (0.83)	12.62 ± 0.43 (0.86)	12.80 ± 0.44 (0.88)
Error-weighted mean age	**11.74 ± 0.28 (0.75)**		**12.06 ± 0.28 (0.77)**	**12.47 ± 0.29 (0.79)**	**12.64 ± 0.30 (0.82)**
East Alnesdalen moraine (Børtjønna)					
ALN 1801*	13.78 ± 0.45 (0.93)	30	14.14 ± 0.46 (0.96)	14.63 ± 0.48 (0.99)	14.87 ± 0.50 (1.02)
ALN 1802	12.56 ± 0.46 (0.87)	30	12.89 ± 0.47 (0.90)	13.34 ± 0.49 (0.93)	13.53 ± 0.50 (0.95)
ALN 1803	12.49 ± 0.42 (0.85)	30	12.82 ± 0.43 (0.87)	13.27 ± 0.44 (0.90)	13.46 ± 0.45 (0.93)
ALN 1804	11.48 ± 0.43 (0.80)	30	11.79 ± 0.44 (0.83)	12.19 ± 0.46 (0.85)	12.36 ± 0.47 (0.88)
Error-weighted mean age	**12.17 ± 0.25 (0.76)**		**12.49 ± 0.26 (0.78)**	**12.92 ± 0.27 (0.81)**	**13.11 ± 0.27 (0.83)**
Alnesdalen rock glacier (Wilson et al., 2020)					
ALN 1805	12.33 ± 0.44 (0.85)	40	12.77 ± 0.46 (0.88)	13.22 ± 0.47 (0.91)	13.41 ± 0.49 (0.94)
ALN 1806	13.65 ± 0.43 (0.92)	40	14.13 ± 0.45 (0.95)	14.63 ± 0.47 (0.98)	14.86 ± 0.48 (1.02)
ALN 1807	13.83 ± 0.54 (0.98)	40	14.33 ± 0.56 (1.02)	14.83 ± 0.58 (1.05)	15.07 ± 0.60 (1.09)
Mean age	**13.27 ± 0.82 (1.13)**		**13.74 ± 0.85 (1.17)**	**14.23 ± 0.88 (1.22)**	**14.45 ± 0.90 (1.25)**
Alnesdalen rock-slope failure					
SB-170810-1	10.54 ± 0.47 (0.78)	30	10.83 ± 0.49 (0.81)	11.21 ± 0.50 (0.83)	11.36 ± 0.52 (0.85)
SB-170810-2	11.47 ± 0.43 (0.80)	30	11.78 ± 0.44 (0.83)	12.19 ± 0.46 (0.85)	12.35 ± 0.47 (0.88)
SB-170810-3	11.44 ± 0.46 (0.82)	30	11.75 ± 0.47 (0.84)	12.16 ± 0.49 (0.87)	12.32 ± 0.50 (0.89)
SB-170810-4	11.43 ± 0.39 (0.78)	30	11.73 ± 0.40 (0.80)	12.14 ± 0.42 (0.83)	12.30 ± 0.43 (0.85)
SB-170810-5	11.70 ± 0.41 (0.81)	30	12.01 ± 0.43 (0.83)	12.43 ± 0.44 (0.86)	12.60 ± 0.45 (0.88)
Error-weighted mean age	**11.35 ± 0.19 (0.70)**		**11.66 ± 0.20 (0.72)**	**12.06 ± 0.20 (0.74)**	**12.22 ± 0.21 (0.76)**
Skarfjelldalen					
ALN 1904	13.49 ± 0.37 (0.88)	40	13.96 ± 0.38 (0.91)	14.61 ± 0.40 (0.95)	14.66 ± 0.40 (0.96)
ALN 1905	13.66 ± 0.39 (0.90)	40	14.13 ± 0.41 (0.93)	14.79 ± 0.43 (0.97)	14.84 ± 0.43 (0.98)
ALN 1906	13.68 ± 0.35 (0.88)	40	14.16 ± 0.36 (0.91)	14.81 ± 0.38 (0.96)	14.87 ± 0.38 (0.96)
ALN 1907	12.74 ± 0.36 (0.84)	40	13.18 ± 0.38 (0.87)	13.79 ± 0.40 (0.91)	13.84 ± 0.40 (0.91)
ALN 1908*	12.16 ± 0.36 (0.80)	40	12.58 ± 0.37 (0.83)	13.17 ± 0.39 (0.87)	13.21 ± 0.39 (0.87)
Error-weighted mean age	**13.39 ± 0.19 (0.81)**		**13.85 ± 0.19 (0.84)**	**14.50 ± 0.20 (0.88)**	**14.50 ± 0.20 (0.88)**
Alnesreset					
ALN 1909	11.24 ± 0.32 (0.74)	30	11.56 ± 0.33 (0.76)	11.94 ± 0.34 (0.78)	11.96 ± 0.34 (0.79)
ALN 1910	11.67 ± 0.32 (0.76)	30	11.98 ± 0.33 (0.78)	12.38 ± 0.34 (0.81)	12.40 ± 0.34 (0.81)
ALN 1911	11.65 ± 0.33 (0.77)	30	11.97 ± 0.34 (0.79)	12.37 ± 0.35 (0.81)	12.39 ± 0.35 (0.81)
ALN 1912	12.33 ± 0.43 (0.85)	30	12.66 ± 0.44 (0.87)	13.08 ± 0.46 (0.90)	13.29 ± 0.47 (0.93)
Error-weighted mean age	**11.65 ± 0.17 (0.71)**		**11.96 ± 0.18 (0.73)**	**12.36 ± 0.18 (0.75)**	**12.39 ± 0.18 (0.76)**
Trollstigen viewpoint					
TROLL-1	11.71 ± 0.38 (0.79)	30	12.04 ± 0.39 (0.81)	12.45 ± 0.40 (0.84)	12.62 ± 0.41 (0.86)
Finnan moraine (Strupen)					
ALN 1901	10.14 ± 0.39 (0.71)	24	10.36 ± 0.39 (0.73)	10.70 ± 0.41 (0.75)	10.73 ± 0.41 (0.75)
ALN 1902	10.30 ± 0.38 (0.72)	24	10.53 ± 0.39 (0.73)	10.89 ± 0.40 (0.76)	10.91 ± 0.40 (0.76)
ALN 1903	10.09 ± 0.35 (0.69)	24	10.30 ± 0.36 (0.71)	10.64 ± 0.37 (0.73)	10.67 ± 0.37 (0.73)
Error-weighted mean age	**10.17 ± 0.21 (0.64)**		**10.32 ± 0.22 (0.65)**	**10.74 ± 0.23 (0.67)**	**10.74 ± 0.23 (0.67)**
Breitinden					
BREI-01	72.47 ± 0.83 (4.43)	N/A			
BREI-02	17.32 ± 0.54 (1.16)	80	18.47 ± 0.58 (1.24)	19.63 ± 0.62 (1.32)	20.06 ± 0.64 (1.38)
BREI-03-A	116.22 ± 2.13 (7.37)	N/A			
BREI-03-B	110.43 ± 1.70 (6.91)	N/A			

Reported are raw ages (uncorrected), ages corrected for uplift, ages corrected for uplift and snow shielding, and final ages corrected for uplift, snow shielding, and erosion. For sites with two or more samples, the 'single landform' tool has been used to detect outliers* and to calculate summary statistics. Error-weighted mean ages are provided, except for the Alnesdalen rock glacier where only a mean age with standard deviation could be calculated. Ages are given with external uncertainties in parenthesis. Additional field, laboratory and calculation details are given in Supplemental Tables S1 and S2. Bold values are the site mean values.

exposure ages than both the West and East Alnesdalen moraines. This was the case for the corrected mean age of 14.5 ± 2.5 ka from the possible rock glacier but not for the corrected mean age of 12.2 ± 1.5 ka from the rock-slope failure. Interpretation of the exposure age of the rock glacier is entirely consistent with our expectation that it formed on terrain that was ice-free when the moraines were deposited in the Younger Dryas Stadial. The younger ^{10}Be exposure age of the rock-slope failure is difficult to

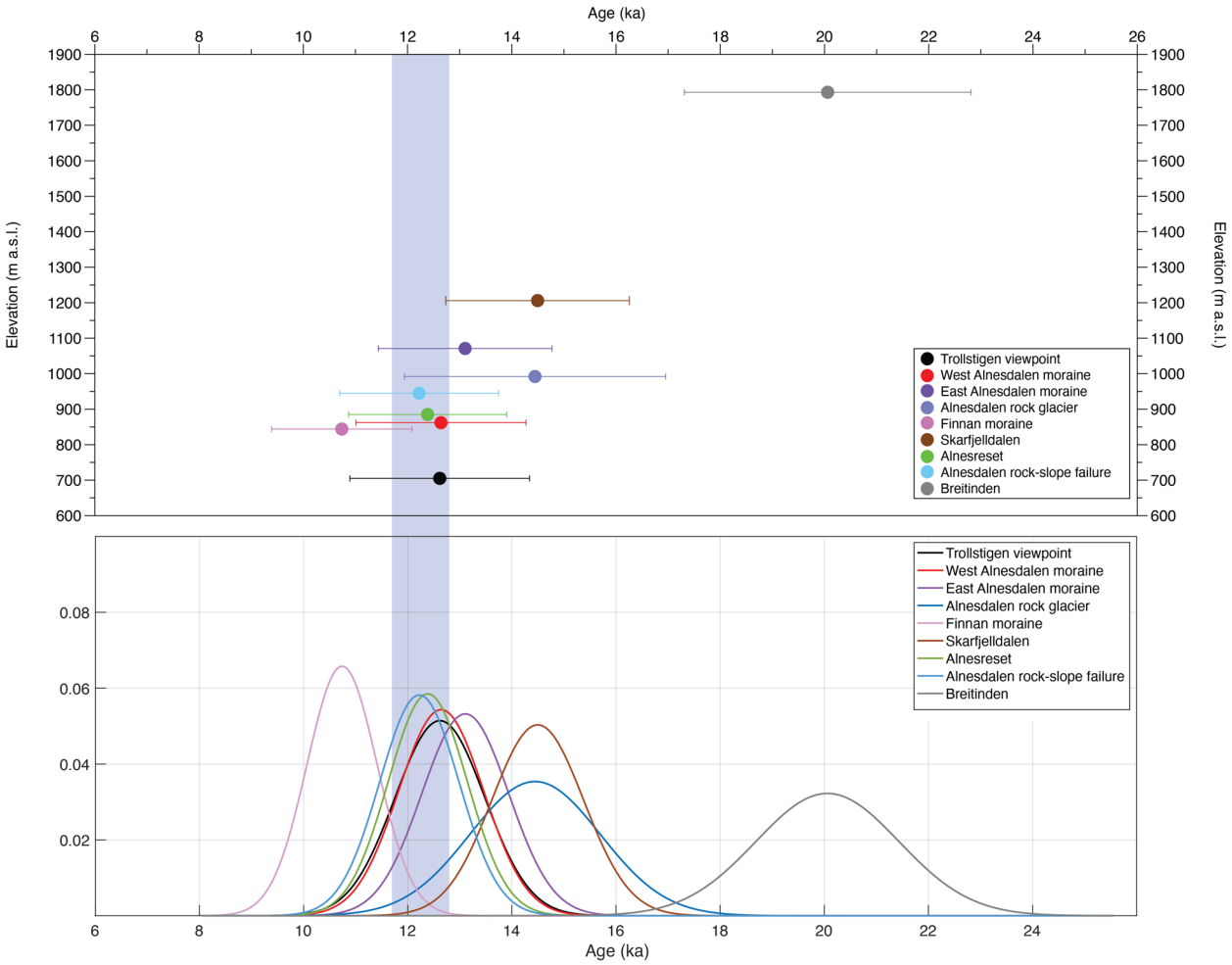

Figure 10. ^{10}Be ages for the nine sites. Upper panel: Elevation distribution of corrected ages with 2σ external uncertainties. Lower panel: Probability density distributions. Mean corrected ages are shown for sites with more than one dated sample. The shaded vertical band spans the Younger Dryas.

explain because, on the basis of its morphostratigraphical position, this feature predates the rock glacier. The most plausible explanation for the relatively young age from the rock-slope failure is post-depositional disturbance of surface boulders, evidenced by the presence of frost-sorted patterned ground (large-scale sorted circles) on the surface of this landform. Snow cover could also be thicker at the site of the rock-slope failure.

SHD ages and their interpretation

SHD ages with their associated 95% confidence intervals from all 121 sites (including sub-sites and control sites) are summarised in Table 4 and visualised in Figure 11. The corresponding *R*-value distributions (Figure 12a–c) have been found particularly useful in identifying, differentiating and interpreting landforms with synchronous surfaces (such as moraines, rock-slope failures and ice-scoured bedrock) from those with diachronous surfaces, such as talus slopes, pronival ramparts and snow-avalanche fans (see, e.g. Matthews and Mourne, 2025; Matthews and Winkler, 2022). Each SHD age provides an estimate of the average age of a land surface. Whereas the SHD age from a synchronous surface can be expected to estimate the timing of the formation of a landform during a single short-lived event, the SHD age of a diachronous surface may provide evidence of landform history but bear little or no relationship to the timing of the onset of landform development (i.e. landform age).

Moraines. Of the 22 sites on moraines, a group of 18 yielded SHD ages between 11.5 ± 1.6 and 14.9 ± 1.7 ka (Table 4; Figure 10). Based on SHD ages and their statistical confidence intervals alone, the results suggest that moraine deposition could have occurred at various times between the Bölling-Allerød Interstadial and the Early Holocene. However, most can be assigned to the Younger Dryas, particularly when interpreted in the light of the available ^{10}Be ages and morphostratigraphy. Almost all of these moraine sites have near-normal *R*-value distributions (Figure 12a), as expected for synchronous surfaces

Three SHD ages from sites 7A, 7B and 8 on the West and East Alnesdalen moraine ridges (also dated by ^{10}Be), range from 11.7 ± 1.4 to 12.8 ± 1.3 ka and are fully compatible with having been deposited during the Younger Dryas Stadial. Three SHD ages from the terminal moraine ridges that are located closely distal to the West Alnesdalen moraine (sites 58 and 105) or proximal to the East Alnesdalen moraine (sites 9A) are closely similar (between 12.8 and 11.5 ka, respectively) and cannot be separated statistically. Although the SHD age from site 9A (14.6 ± 1.6 ka) is statistically older than that of site 9B from the same ridge, it is younger according to morphostratigraphy. Thus, the SHD age of site 9B is considered an anomaly and all four moraine ridges from mid and upper Alnesdalen are assigned to the Younger Dryas Stadial.

Three lateral moraine ridges in lower Alnesdalen can also be assigned to the Younger Dryas on the basis of SHD ages. Two of

Table 4. Schmidt hammer *R*-values, SHD exposure ages and related statistics for all sites classified according to landform type.

Landform type	Site no.	Mean *R*-value	S.D.	*N*	C.I. (95%)	Skew	Kurtosis	Age (years)	C.I. (95%)	*Cs* (years)	*Cc* (years)
Moraine	7A	40.2	9.67	175	1.44	0.20	−0.33	11,650	1400	1075	900
	7B	39.1	9.33	200	1.31	−0.11	−0.12	12,465	1320	965	900
	1	56.4	11.0	200	1.55	−0.56	−0.57	−360	1475	1140	935
	2	55.5	8.14	200	1.14	−0.65	0.19	310	1260	845	935
	34A	35.8	10.06	100	1.99	0.34	−0.41	14,910	1735	1485	890
	34B	38.1	9.58	100	1.90	0.06	−0.77	13,205	1655	1415	860
	35	36.0	9.32	200	1.31	0.27	−0.81	14,765	1315	965	890
	8	38.6	8.30	200	1.17	0.03	−0.80	12,835	1245	860	895
	9A	36.2	8.85	100	1.75	0.14	−0.79	14,615	1585	1310	890
	9B	40.4	9.01	100	1.79	−0.27	−0.79	11,500	1605	1330	895
	46	38.8	8.60	200	1.21	−0.03	−0.65	12,685	1265	890	900
	47	39.5	8.39	200	1.18	−0.23	−0.67	12,170	1250	870	900
	51	55.2	7.73	200	1.09	−0.16	−0.25	530	1230	800	935
	58	38.7	8.80	150	1.42	0.14	−0.83	12,760	1385	1055	900
	105	38.7	7.64	150	1.23	−0.14	−0.71	12,760	1285	915	900
	62	37.7	7.06	200	0.99	−0.09	−0.48	13,505	1155	730	895
	64	37.0	8.79	200	1.24	0.25	−0.85	14,020	1275	910	895
	71	38.7	8.76	200	1.23	0.09	−0.61	12,760	1275	910	900
	78	38.0	7.94	200	1.12	0.07	−0.46	13,280	1215	825	895
	79	38.2	8.19	200	1.15	0.13	−0.55	13,132	1235	850	895
	80	51.0	8.79	200	1.24	−0.39	−0.13	3645	1295	910	925
	99	39.3	8.29	200	1.17	0.07	−0.86	12,315	1245	860	900
Alluvial fan	3	61.8	7.10	100	1.41	−0.58	0.11	−1715	1245	920	840
	4	57.1	8.30	100	1.64	-1.00	1.08	1340	1365	1075	840
	36	57.5	8.77	200	1.23	−0.46	−0.37	1080	1160	800	840
	67	40.0	8.53	200	1.20	0.19	−0.53	12,465	1145	775	845
Pronival rampart	32	41.19	8.69	150	1.41	−0.35	−0.56	10,915	1380	1045	905
	5	38.9	8.64	150	1.39	−0.02	−0.23	12,615	1370	1035	895
	6	36.8	10.17	150	1.64	−0.06	−0.54	14,170	1510	1220	895
	28	39.0	8.62	200	1.20	−0.01	−0.53	12,540	1265	895	900
	29	44.7	11.66	200	1.63	−0.02	−0.76	8315	1515	1210	910
	30	45.8	9.88	200	1.38	−0.11	−0.61	7500	1370	1025	915
	14	43.9	9.77	200	1.37	−0.05	−0.47	8905	1360	1010	910
	10	36.9	8.91	200	1.25	0.37	0.00	14,095	1285	925	895
	12A	36.1	9.31	100	1.85	0.00	−0.97	14,690	1640	1375	890
	12B	38.7	8.86	100	1.76	0.06	−0.76	12,760	1590	1310	900
	96	38.3	9.48	200	1.33	0.37	−0.15	13,060	1330	980	895
Rock glacier?	24	37.7	8.34	200	1.17	0.03	−0.60	13,500	1245	865	895
	25	39.2	8.35	200	1.17	0.33	0.16	12,390	1245	865	900
	26	38.0	9.24	200	1.29	0.05	−0.42	13,380	1310	960	895
	104	38.2	8.57	200	1.20	−0.24	−0.33	13,130	1260	890	895
Talus slope	27	46.2	9.78	200	1.37	−0.19	−0.27	7200	1365	1015	915
	31	51.7	9.19	200	1.28	−0.28	−0.58	3125	1330	950	925
	15	48.8	8.68	200	1.22	−0.28	−0.44	5275	1285	900	920
	11	48.9	8.81	200	1.24	−0.19	−0.33	5200	1295	915	920
	13A	46.8	9.79	100	1.94	−0.04	−0.97	6755	1710	1445	915
	13B	42.6	9.43	100	1.87	0.12	−0.53	9870	1660	1395	905
	45A	49.0	8.76	100	1.74	−0.10	−0.80	5125	1590	1295	920
	45B	46.0	8.53	100	1.69	−0.03	−0.50	7350	1555	1260	915
	84	45.0	8.30	200	1.17	0.04	−0.37	8090	1255	860	910
	92A	47.4	9.68	100	1.92	−0.59	−0.34	6315	1700	1430	915
	92B	45.2	10.78	100	2.14	−0.50	−0.40	7945	1835	1595	910
Snow-avalanche fan	43	50.5	8.71	200	1.22	−0.27	−0.13	4015	1290	905	925
	44	49.5	8.91	185	1.29	−0.30	−0.37	4755	1330	960	920
	54	40.8	9.31	200	1.31	−0.12	−0.33	11,205	1320	965	900
	74	45.4	8.53	200	1.23	0.03	−0.47	7795	1270	885	910
	75	47.6	7.74	200	1.09	0.04	0.04	6165	1220	800	915
Rock-slope failure	20	38.9	8.13	200	1.14	0.0	−0.48	12,615	1230	840	900
	21	38.2	7.86	200	1.10	−0.20	−0.40	13,130	1210	815	895
	22	38.3	8.05	200	1.13	−0.20	−0.51	13,060	1225	835	895
	23	38.6	8.40	200	1.17	0.03	−0.66	12,835	1250	870	895
	41	42.7	8.93	200	1.26	0.02	−0.34	9795	1295	925	905
	42A	44.3	9.90	100	1.96	0.17	−0.71	9350	1720	1465	905
	42B	40.8	9.38	100	1.86	0.27	−0.26	11,205	1655	1385	900

(continued)

Table 4. (continued)

Landform type	Site no.	Mean *R*-value	S.D.	*N*	C.I. (95%)	Skew	Kurtosis	Age (years)	C.I. (95%)	*Cs* (years)	*Cc* (years)
Rock-slope failure	48	41.7	9.51	200	1.34	0.02	−0.30	10,540	1335	985	905
	52	35.7	9.01	200	1.27	0.38	−0.65	14,985	1290	935	890
	53	36.9	8.30	200	1.17	0.18	−0.44	14,095	1240	860	895
	55	36.7	8.89	200	1.25	0.30	−0.46	14,245	1285	920	895
	81	39.4	8.05	200	1.13	−0.05	−0.52	12,245	1225	835	900
	82	39.8	7.51	200	1.06	0.01	−0.27	11,945	1190	780	900
Boulder field	56	36.0	8.03	200	1.13	0.01	−0.75	14,765	1220	830	890
	101	40.4	8.28	200	1.16	0.11	−0.61	11,500	1245	860	900
Boulders on till	76	37.7	8.60	200	1.21	0.20	−0.69	13,505	1265	890	895
	95	36.3	8.75	200	1.23	0.29	−0.61	14,540	1270	905	890
Boulders on bedrock	73	36.4	8.04	200	1.13	0.40	−0.32	14,465	1225	835	900
	89	40.1	9.85	200	1.39	0.27	−0.74	11,725	1360	1020	900
Boulder pavement	49	39.2	8.21	200	1.15	0.21	−0.59	12,390	1235	850	900
	59	39.9	8.31	200	1.17	−0.28	−0.40	11,870	1245	860	900
	60A	35.3	8.84	100	1.75	0.44	0.51	15,280	1590	1305	905
	60B	40.5	8.05	100	1.60	−0.18	−0.25	11,425	1495	1190	900
Patterned ground	16	40.5	9.17	200	1.29	0.13	−0.56	11,425	1310	950	900
(sorted circles)	17	36.3	9.57	200	1.35	0.10	−0.41	14,540	1335	990	890
	18	38.6	9.52	200	1.34	0.33	−0.29	12,835	1335	985	895
	19	40.8	8.79	200	1.24	−0.11	−0.76	11,205	1280	910	900
	98	40.1	8.39	200	1.18	0.06	−0.69	11,725	1250	870	900
Solifluction lobe	61	36.0	8.54	200	1.20	0.07	−0.49	14,765	1255	885	890
	100	41.3	9.06	200	1.27	−0.08	−0.60	10,835	1305	940	905
Glacially-scoured bedrock	33A	40.5	10.68	100	2.12	0.08	−0.61	12,140	1625	1385	845
	33B	35.9	10.18	100	2.02	0.15	−0.41	15,135	1570	1320	845
	40	39.7	8.60	200	1.21	−0.08	−0.73	12,660	1150	780	845
	106	33.3	8.44	200	1.19	0.48	−0.04	16,825	1140	770	845
	107	33.3	8.14	200	1.14	0.33	−0.03	16,825	1125	740	850
	108	32.1	8.57	200	1.21	0.56	0.25	17,605	1150	780	845
	37	41.4	9.00	200	1.27	0.05	−0.28	11,555	1175	820	845
	38A	41.6	7.94	100	1.57	−0.19	−0.08	11,425	1330	1030	845
	38B	39.2	8.13	100	1.61	−0.05	−0.72	12,985	1350	1055	845
	39	41.4	8.83	200	1.24	−0.09	−0.56	11,555	1165	805	845
	50	60.2	6.70	200	0.94	−0.73	0.42	675	1035	610	840
	57	35.9	8.06	200	1.13	0.13	−0.32	15,135	1120	735	845
	63	35.8	7.39	200	1.04	0.32	−0.44	15,200	1080	670	845
	65	36.9	8.21	200	1.15	0.29	−0.53	14,480	1130	745	845
	66	37.0	8.11	200	1.14	0.13	−0.68	14,415	1125	740	845
	69	38.0	8.16	200	1.15	−0.09	−0.53	13,765	1125	740	845
	70	37.7	9.28	200	1.31	0.19	−0.52	13,960	1195	845	845
	72	35.3	9.05	200	1.27	0.46	−0.55	15,520	1155	785	845
	83A	38.7	8.06	100	1.60	0.01	−0.28	13,310	1345	1045	845
	83B	42.8	7.90	100	1.57	−0.26	−0.15	10,645	1330	1025	845
	85	37.6	8.02	200	1.13	0.12	−0.81	14,025	1115	730	845
	86	38.7	8.05	200	1.13	0.16	−0.75	13,310	1120	730	845
	87	39.4	7.72	100	1.53	0.22	0.15	12,855	1310	1000	845
	90A	39.6	7.94	100	1.57	−0.19	−0.44	12,725	1335	1030	845
	90B	37.3	8.99	100	1.78	0.34	−0.23	14,220	1440	1165	845
	91	39.8	7.87	200	1.11	0.03	−0.73	12,595	1110	715	845
	93	39.9	9.52	200	1.34	−0.18	−0.74	12,530	1210	865	845
	94A	42.4	8.47	100	1.68	−0.33	−0.60	10,905	1405	1125	845
	94B	39.6	8.49	100	1.68	0.08	−0.06	12,725	1390	1100	845
	102	44.8	8.02	200	1.13	−0.42	−0.17	9345	1115	730	845
Snow-avalanche-scoured bedrock	88A	59.1	8.02	100	1.60	−1.18	1.43	50	1335	1040	840
	88B	62.4	5.84	100	1.16	−1.02	1.40	−2105	1130	760	840
Road-cut bedrock	68	55.2	7.07	200	0.99	−0.38	−0.18	530	1185	735	935
	77	56.9	5.10	100	1.02	−0.13	−0.40	730	1200	755	935

these (sites 62 and 64), which occur on the east-facing valley-side slope of Finnan, yielded SHD ages of 13.5 ± 1.2 and 14.0 ± 1.3 ka respectively. Closely similar SHD ages were obtained from sites 46 and 47 on the lateral moraine located near the base of the northwest-facing slope of Skarfjellenden (Figure 1). SHD ages of 13.3 ± 1.2, 13.1 ± 1.2, and 12.3 ± 1.3 ka for 3 terminal moraines near the head of Skarfjelldalen (sites 78, 79 and 99, respectively, Figure 2), can also be assigned to the Younger Dryas with confidence.

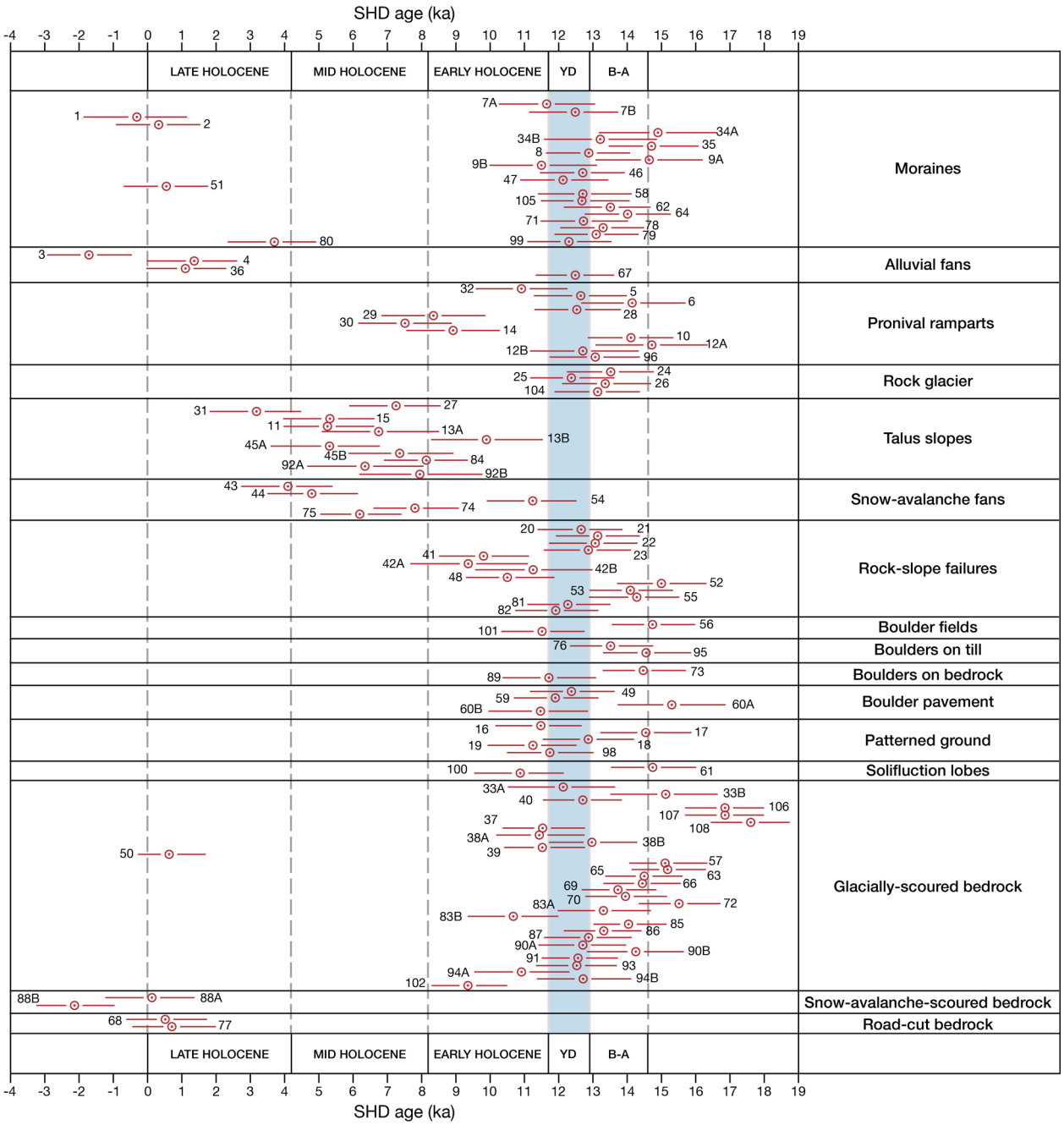

Figure 11. SHD ages with their 95% confidence intervals for each site numbered and grouped according to landform type.
YD: Younger Dryas Stadial (shaded vertical band); BA: Bölling-Allerød Interstadial.

The SHD age of 14.8 ± 1.3 ka from site 35 on a southern laterotermiinal moraine of the South Finnan Glacier (Figure 2) is regarded as anomalously old because: (1) it is morphostratigraphically younger than the older Younger Dryas lateral moraines on the valley side; (2) it is significantly older than the ^{10}Be age of 10.8 ± 1.4 ka obtained from the equivalent northern laterotermiinal moraine; and (3) its positively skewed *R*-value distribution (Figure 12a) suggests that relatively old surface boulders may have been incorporated during moraine formation (possibly derived from boulders of supraglacial origin with a pre-depositional weathering signal).

Disparate SHD ages of 14.9 ± 1.7 and 13.2 ± 1.7 ka (sites 34A and 34B, respectively) were obtained from the short laterotermiinal moraine that was deposited by a former glacier that flowed out of the hanging valley currently occupied by the North Finnan Glacier and Bispevatnet (Figure 2). The positive skew of the *R*-value distribution from site 34A again suggests the possibility that relatively old surface boulders have affected the SHD age of this site. As this moraine appears to merge with the valley-side lateral moraines of approximately the same age, it too is interpreted as dating from the Younger Dryas based on the age of site 34B. The short terminal moraine that relates to a former cirque glacier on the east-facing flank of Alnestinden (site 71) yielded a SHD age of 12.8 ± 1.3 ka, which is interpreted as also dating from the Younger Dryas.

The remaining group of four moraines with SHD ages between −0.4 ± 1.5 and 3.7 ± 1.3 ka (sites 1, 2, 51 and 80), which lie close to the South Finnan Glacier and another present-day glacier in Skarfjelldalen, clearly date from the Late-Holocene. The first three of the sites with SHD ages of −0.4 ± 1.5 to 0.5 ± 1.2 ka are from

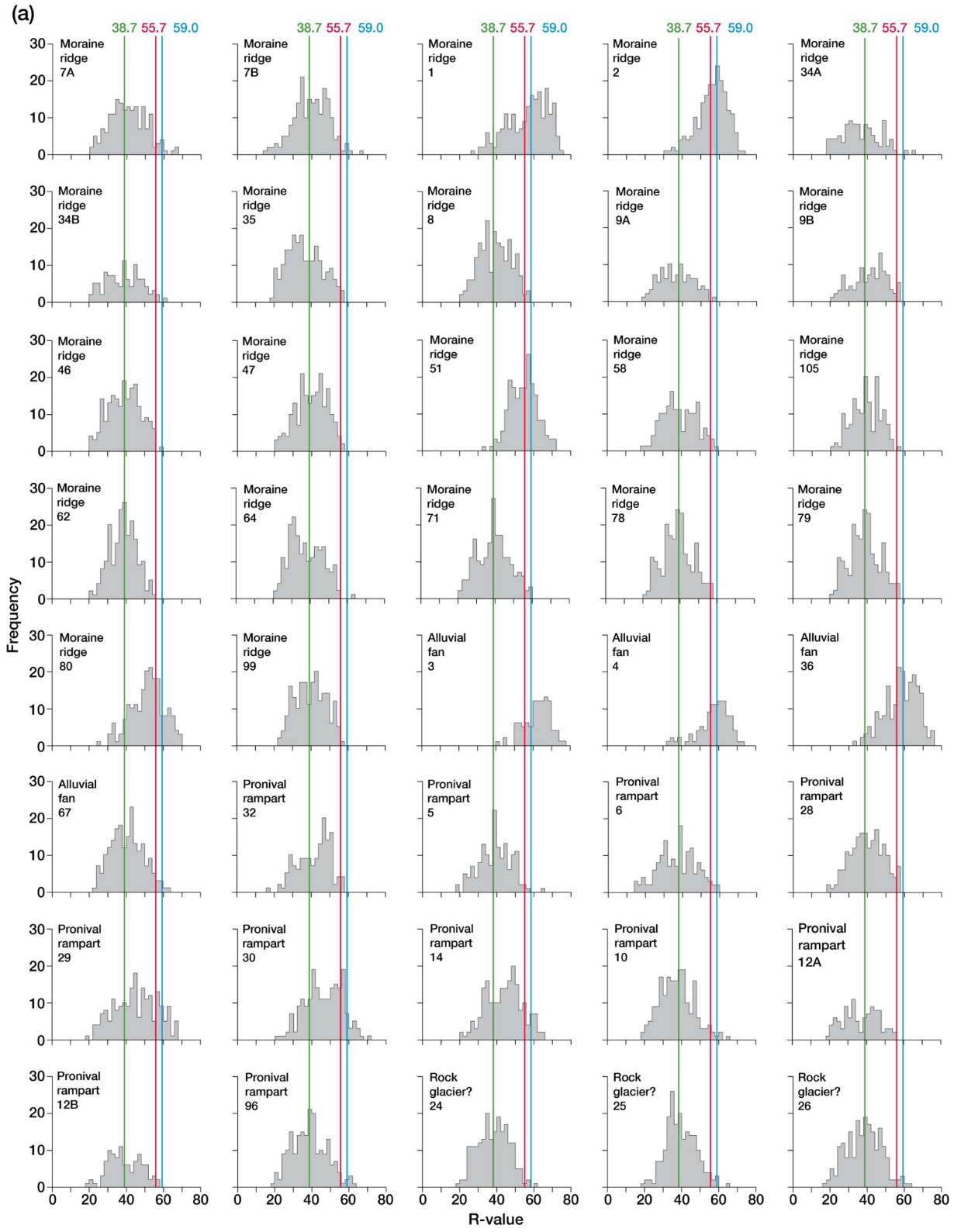

Figure 12. *(continued)*

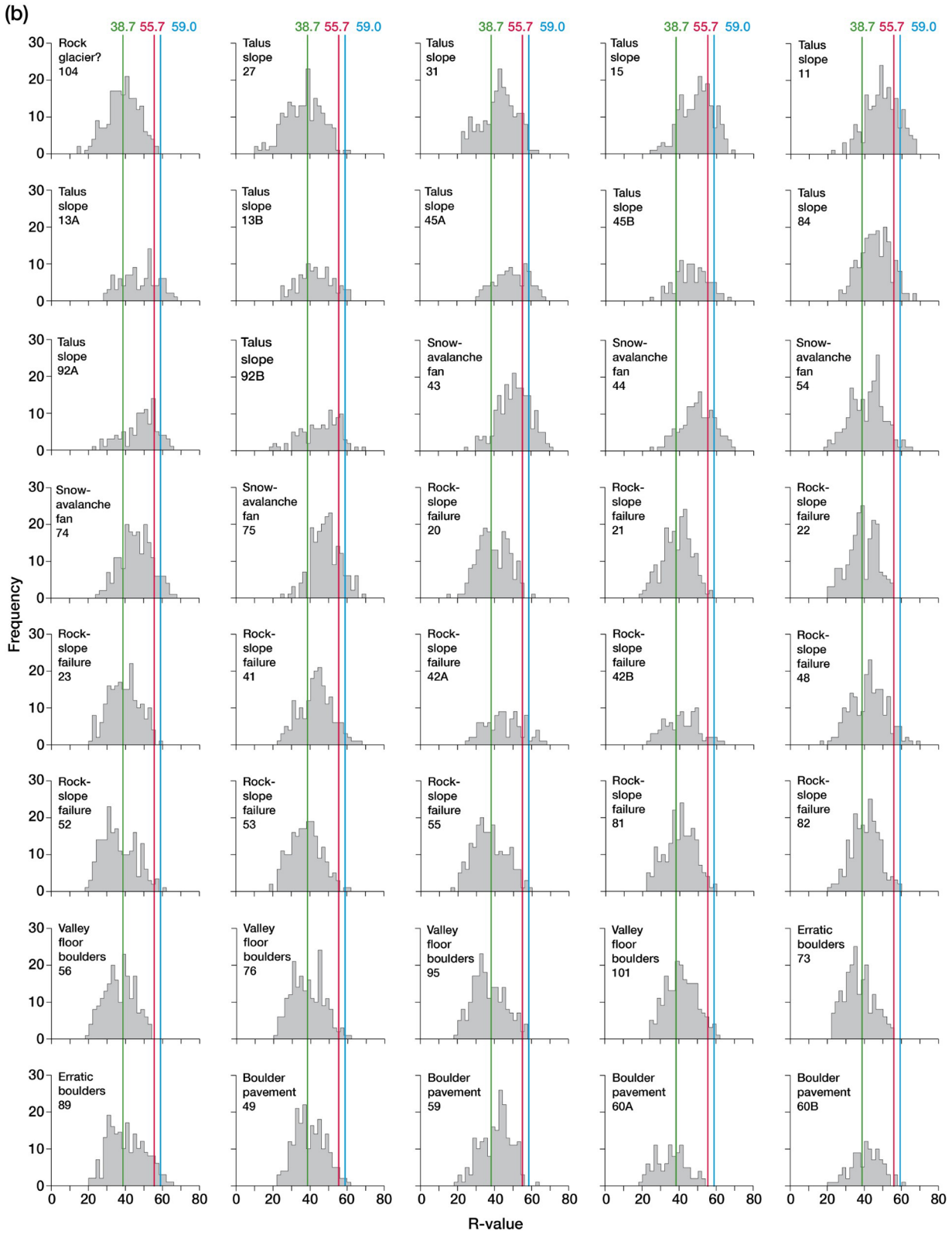

Figure 12. *(continued)*

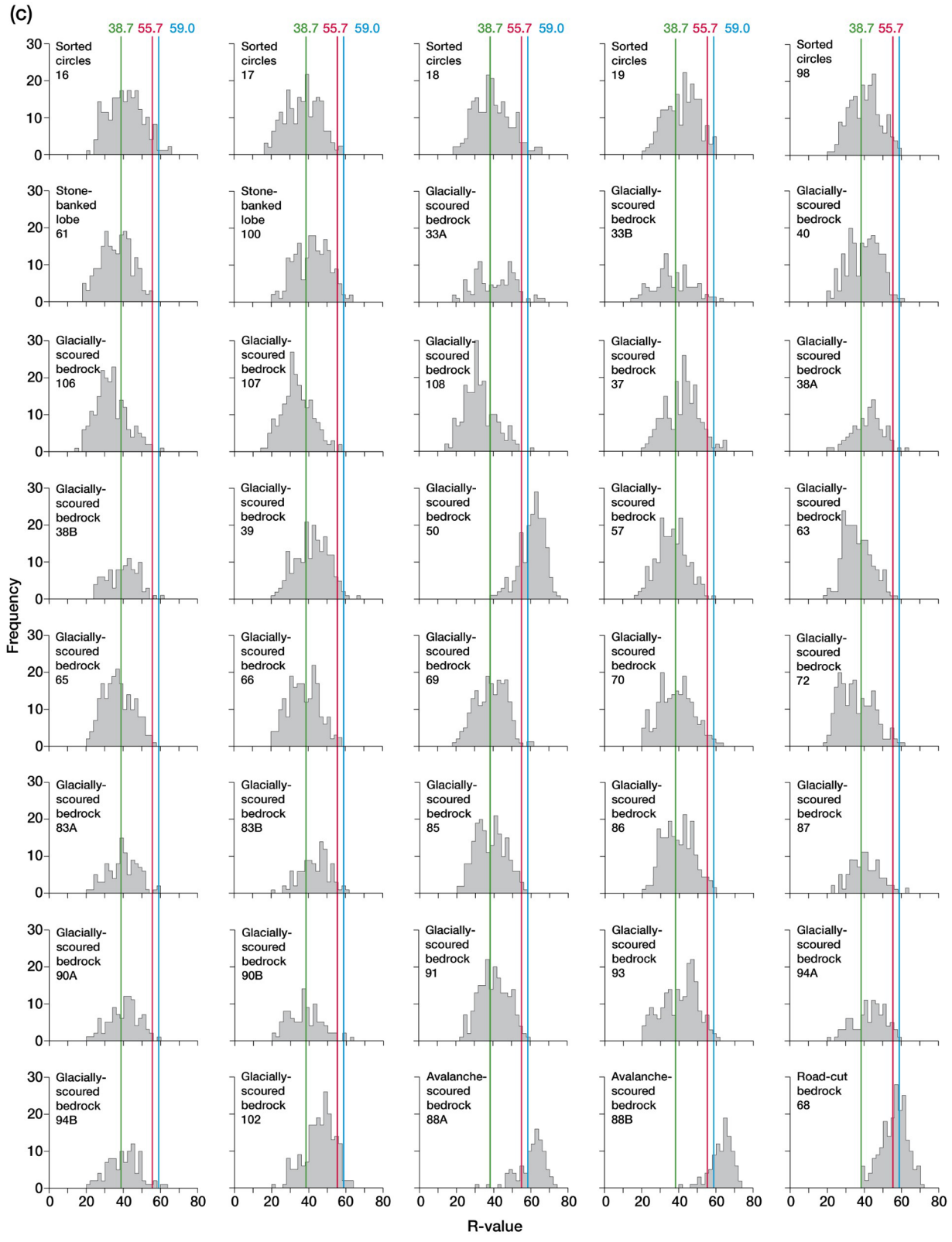

Figure 12. (a–c) Frequency histograms of Schmidt-hammer *R*-values obtained from landform surfaces (note the 2-unit class interval). Vertical lines show mean *R*-values for surfaces of known age (control surfaces for age-calibration). Young control points are represented by glacially-scoured bedrock and alluvial (glaciofluvial) boulders (blue) or moraine boulders and road-cut bedrock (red). Corresponding old control points of 39.0 and 38.4 (statistically indistinguishable and too close to be represented separately) are shown as a single line (38.7, green). See text for further explanation.

the 'Little Ice Age' moraines on the glacier foreland of the South Finnan Glacier (Figures 2 and 6a), which were used as young control points. The significantly older SHD age of 3.7 ± 1.3 ka from site 80 is the closest terminal moraine to the very small glacier at the head of Skarfjelldalen (Figures 3 and 6d). However, we consider that this moraine also dates from the 'Little Ice Age', the relatively old SHD age being caused by anomalously low *R*-values resulting from the short supraglacial or englacial rather than subglacial transport paths that must have characterised the boulders in the moraine. Due to an absence of abrasion, such boulders tend to have a rough surface texture that would result in anomalously low *R*-values for recently exposed surfaces (Boulton, 1978; Matthews, 1987; Olsen et al., 2020). An older moraine, reworked in the 'Little Ice Age' or with the addition of more recent surface rockfall boulders on its surface, is also a possibility.

Alluvial fans. The three active alluvial fans associated with the glacial meltwater stream from the South Finnan Glacier were used as young control surfaces and are essentially modern (sites 3, 4 and 36; Figure 11). The SHD ages of –1.7 ± 1.3 to 1.3 ± 1.4 ka give a good indication of the age resolution to be expected from the application of SHD to smooth, abraided rock surfaces that are unweathered, which can be largely attributed to the variable nature of the gneissic lithology.

Located where the tributary stream from Bispevatnet meets the main valley floor (Figure 1), site 67 yielded a SHD age of 12.5 ± 1.2 ka. This indicates a relict landform which, on the basis of its very large boulders (commonly 2–3 m diameter) must have been deposited by a meltwater stream with much greater discharges than today.

Pronival ramparts. Eleven sites relate to pronival ramparts, which occur widely in the catchment towards the base of steep slopes. Their SHD ages range from 7.5 ± 1.4 to 14.7 ± 1.6 ka (Figure 11). Some of these have been mapped previously (Carlson et al., 1983) and based on their SHD ages and *R*-value distributions, both active and relict examples have been recognised (see Matthews and Wilson, 2015; Wilson et al., 2020).

Pronival ramparts are particularly well developed on both the north and south side of upper Alnesdalen (Figure 3). The northern example (sites 10, 12A, 12B and 14), which extends for about 1.0 km with distal slopes that rise up to 50 m above the valley floor, yielded ages from 8.9 ± 1.5 to 14.7 ± 1.6 ka. As the feature is located distal to the East Alnesdalen moraine on terrain that was deglaciated prior to the Younger Dryas, the older SHD dates suggest parts of the feature have been relict since then. Sites with younger ages, on the other hand, are indicative of later activity, as was suggested for the southern feature (Figure 7a and b) by Wilson et al. (2020) where sites 28, 29 and 30 yielded slightly younger SHD ages of 7.5 ± 1.4 to 12.5 ± 1.3 ka. Although this may indicate that greater rockfall activity occurred during the Holocene on the north-facing valley side, significant later activity has occurred locally on both aspects.

The distributions of *R*-values (Figure 11a) and the relatively young SHD ages of associated talus slopes (see below) support the diachronous nature of many of the pronival rampart surfaces. Site 30, for example, with the youngest SHD age, has a distinct bimodal distribution with the younger mode coinciding with the mean *R*-value of a modern surface and the older mode coinciding with the mean *R*-value of a surface of Younger Dryas age. We conclude therefore that some pronival ramparts remain active today.

The remaining three pronival ramparts (sites 5, 6, 32 and 96) yielded SHD ages between of 14.2 ± 1.5 and 10.9 ± 1.4. The strong negative skew of the *R*-value distribution for the youngest of these (site 32) at the foot of Alnestinden, combined with field evidence of recent snow-avalanche activity nearby (see below) again indicates a diachronous surface. Older ages at the other three sites again suggest features that have been relict since at least the Younger Dryas on terrain located beyond the limits of Younger Dryas glaciers.

Rock glacier. The possible rock glacier in upper Alnesdalen (Figures 3 and 7a) yielded consistent SHD ages between 13.5 ± 1.3 and 12.4 ± 1.3 (sites 24, 25, 26 and 104), which cannot be distinguished statistically (Figure 11). These ages are compatible with the mean corrected ^{10}Be age of 14.5 ± 2.5 ka from this feature. The *R*-value distributions of the four sites are close to normal with no evidence of diachronous surfaces (Figure 12a).

Interpretation of these exposure ages follows Wilson et al. (2020). Initially, following deglaciation in the Bölling-Allerød Interstadial, paraglacial boulder deposition probably involved one or more rock-slope failures. Rock glacier deformation may have occurred in a later phase of development, in a permafrost environment during the Younger Dryas. If this landform is indeed a rock glacier, the surface boulders are likely to have been transported in a largely undisturbed state (cf. Rode and Kellerer-Pirklbauer, 2012; Winkler, 2025; Winkler and Lambiel, 2018) while permafrost creep continued beneath the surface for some time into the Holocene until the landform became relict throughout.

Talus slopes. The 11 sites on talus slopes yielded SHD ages between 9.9 ± 1.7 and 3.1 ± 1.3 ka (Table 4). Pre-Holocene ages can be ruled out statistically (Figure 11): nine sites date from the Mid-Holocene; one from the Early Holocene; and one from the Late-Holocene. The talus slopes are best developed in areas of the landscape that were deglaciated before the Younger Dryas, especially those in upper Alnesdalen. All the dated talus sites are interpreted as diachronous surfaces. Some exhibit significant differences in age between subsites (sites 13A/B, 45A/B and 92A/B; Table 4), which suggest more than one generation of boulders affected different parts of the same surface. Many have appreciable numbers of boulders with *R*-values >60 (sites 11, 13A, 15, 45A, 92A; Figure 12b), which indicate surfaces influenced by significant modern activity. However, as the SHD ages indicate the average exposure age of the surface boulders, a high proportion of the surface boulders (and an even higher proportion of the subsurface material) must be older than Mid-Holocene.

Snow-avalanche fans. Five snow-avalanche fans have SHD ages of 14.0 ± 1.3 to 11.2 ± 1.3 ka (sites 43, 44, 54, 74 and 75; Table 4 and Figure 11). These are located within the areas shown as talus slopes on Figures 2 and 3. Indeed, some snow-avalanche fans are reworked talus slopes. Although different processes are involved (snow-avalanche vs rockfall) both landform types are characterised by diachronous surfaces and their SHD ages are interpreted in much the same way. Low-level modern activity is evident on all five snow-avalanche fans, which reflects the likelihood that only a small quantity of rock particles is transported by each snow avalanche (cf. Matthews et al., 2020a). Snow avalanches are therefore thought to have contributed incrementally to fan development, possibly with varying frequency, over a long period of time.

Rock-slope failures. With SHD ages ranging from 9. 4 ± 1.7 to 15.0 ± 1.3 ka, most of the 13 sites from 8 rock-slope failures date from before the Holocene (Figure 11). The ages of the 3 oldest of these landforms (sites 52, 53 and 55), which are located in upper Alnesdalen, exceed 14.0 ka, while 4 sites from different transverse ridges on the tongue-shaped feature (sites 20, 21, 22 and 23), also in upper Alnesdalen, yielded ages between 12.6 ± 1.2 and

13.1 ± 1.2 ka (see Wilson et al., 2020). Thus, the four oldest rock-slope failures, all of which are relatively large, occurred <1–2 ka after deglaciation. One of these, site 55, includes the Alnesstein shown in Figures 4a and 8.

Two sites from a rock-slope failure in upper Skarfjelldalen (sites 81 and 82) yielded slightly younger SHD ages of 12.3 ± 1.2 and 12.0 ± 1.2 ka. This rock-slope failure is morphostratigraphically older than the moraine ridge (sites 78 and 79) that overrides it, which has been dated to the Younger Dryas Stadial.

Three relatively small rock-slope failures near Alnesreset (sites 41, 42A, 42B and 48; Figure 2) with a SHD age range of 9.4 ± 1.7 to 11.2 ± 1.7 ka date from the Early Holocene. These SHD ages appear slightly younger than the ^{10}Be mean age of 12.4 ± 1.5 ka obtained from glacially-scoured bedrock nearby.

Boulder fields. The two boulder fields (sites 56 and 101) in upper Alnesdalen and upper Skarfjelldalen (Figures 3 and 8b) respectively, produced significantly different SHD ages of 14.8 ± 1.2 and 11.5 ± 1.3 ka. The older age indicates formation and stabilisation shortly after deglaciation while the younger age suggests later disturbance before stabilisation in the Early Holocene.

Boulders on till. Glacially-transported boulders embedded in till surfaces were dated in mid-Alnesdalen (site 76; Figure 3) and south of Bispevatnet (site 95; Figure 2). Both sites are located on the proximal side of dated moraine ridges and interpreted as having been deposited as glaciers retreating from moraines at the end of the Younger Dryas. The SHD age of 13.5 ± 1.3 ka from site 76 cannot be distinguished statistically from the mean ^{10}Be age of 12.7 ± 1.6 ka from site 7 on the West Alnesdalen moraine. The SHD age of 14.5 ± 1.3 from site 95 is considered anomalously old and attributable to local lithological variation (see further discussion below).

Boulders on bedrock. Glacially-transported boulders perched on glacially-scoured bedrock surfaces yielded SHD ages of 14.5 ± 1.2 ka (site 73) and 11.7 ± 1.4 ka (site 89; Figures 2 and 11). The corresponding SHD ages from each underlying bedrock surface were 15.5 ± 1.2 (site 72), 12.7 ± 1.3 (site 90A) and 14.2 ± 1.4 (sites 90B). The results from sites 89 and 90A, which lie proximal to Younger Dryas moraine ridges (sites 46 and 47), are fully consistent with deposition of boulders during withdrawal of the glacier from the moraine. However, the large variation in SHD ages both within and between the other surfaces of demonstrably similar age, again point to large potential errors caused by local lithological variability within the Alnesdalen catchment.

Boulder pavements. SHD ages from three of the four boulder-pavement sites in upper Alnesdalen (sites 49, 59 and 60B, Figure 3; see also Figure 8c) fall within a relatively narrow range (11.4 ± 1.5 to 12.4 ± 1.2 ka) and cannot be distinguished statistically from each other (Figure 11). These ages are consistent with formation throughout the Bölling-Alleröd Interstadial and Younger Dryas Stadial. The anomalously old SHD age of 15.3 ± 1.6 ka from site 60A may have been affected by anomalously high moisture availability leading to enhanced weathering of boulder surfaces.

Patterned ground. The SHD age range of 14.5 ± 1.3 to 11.2 ± 1.3 ka from the sorted circles in upper Alnesdalen (sites 16–19) and upper Skarfjelldalen (site 98; Figure 3; see also Figures 8a and 11) may reflect the time span between the onset and final stabilisation of these landforms (cf. Winkler et al., 2016, 2020). The dating evidence suggests that they formed rapidly following deglaciation, that some sites remained active during the Younger Dryas and that final stabilisation occurred before the Holocene Thermal Maximum (see further discussion below).

Solifluction lobes. The SHD ages of 14.8 ± 1.3 and 10.8 ± 1.3 ka from two stone-banked solifluction lobes (sites 61 and 100; Figure 3) exhibit a similar age range to the sorted circle sites (see also Figure 11). Nevertheless, interpretation must differ as gelifluction rather than frost sorting is the primary formation process. Gelifluction would have been favoured by water-saturated conditions during deglaciation in the Bölling-Allerød Interstadial but may have continued at a reduced rate long into the Holocene while boulders remained almost undisturbed on the lobe surface (cf. Matthews et al., 1986a; Nesje et al., 1989).

Glacially-scoured bedrock. Apart from the modern control surface from the glacier foreland of the South Finnan Glacier (site 50) with a SHD age of 0.7 ± 1.0 ka, 29 glacially-scoured bedrock sites ranged in age between 9.4 ± 1.1 and 17.6 ± 1.2 ka (Figure 11). Most of the sites occur within the extensive area of bedrock highlighted on Figure 2, which we interpret as having been occupied by glacier ice in Younger Dryas times. The very wide range of SHD ages from these glacially-scoured bedrock sites seems to be greatly affected by non-age related factors (see below).

SHD ages of 16.8 ± 1.1 to 17.6 ± 1.2 ka for sites 106, 107 and 108, which are clearly anomalously old, can be attributed to the presence of a particularly weak (schistose) lithology, possibly combined with the survival of pre-weathered surfaces (i.e. weathered surfaces inherited from before the bedrock was scoured by Younger Dryas glaciers). Excluding these 3 anomalies, 26 of the bedrock sites have SHD ages that are no older than 15.2 ± 1.1 ka (site 63). Taking the confidence intervals into account, a pre-Younger Dryas exposure age can be ruled out for only six of these (sites 37, 38A, 39, 83B, 94A and 102; Figure 11). In contrast, the youngest of the SHD ages from these glacially-scoured sites may have been affected by an anomalously high loss of weathered material from the rock surfaces since the glacial scouring occurred.

Snow-avalanche scoured bedrock. Site 88 is uniquely affected by snow-avalanche scour. It is located at the foot of Alnestinden (Figure 2), a few metres away from and alongside the glacially-scoured bedrock site 90 that is protected from snow avalanches by an overhanging cliff face. The avalanche-prone site is characterised by scattered very angular rock fragments and finer material from modern avalanches. The SHD ages of 0.1 ± 1.3 ka (site 88A) and –2.1 ± 1.1 ka (site 88B) from the avalanche-prone site, combined with their *R*-value distributions (Figure 12b) provide evidence not only of the existence of recent avalanche activity but also of the potential effectiveness of snow-avalanche erosion. The *R*-value distribution of the avalanche-scoured bedrock site 88A is remarkably similar to the modern glacially-scoured bedrock site 50. We attribute the difference of ~2 ka between the SHD ages of sites 88A and 88B to the patchy nature of snow-avalanche scour.

Road-cut bedrock. Sites 68 and 77 from road cuts (Figures 2 and 11), both of which were used as modern control surfaces, yielded SHD ages of 0.5 ± 1.2 and 0.7 ± 1.3 ka, respectively.

Discussion

Late Glacial and Holocene glacial history

Our ^{10}Be and SHD ages from ice-marginal moraines and glacially-scoured bedrock enable a detailed reconstruction of the sequence of glacial events in space and time. In general, the two sets of exposure ages are complementary within comparable millennial-scale levels of uncertainty. The broad framework from the

Last Glacial Maximum to the Early Holocene is provided by the ^{10}Be ages, while confirmation and further details for the Late Glacial to Late-Holocene are contributed by SHD ages.

Our preferred ^{10}Be age for the deglaciation of the highest point in the drainage basin (Breitinden) of ~20 ka is a broad approximation that is particularly uncertain given the lack of an accurate uplift correction for samples of this age. Deglaciation at this time is consistent with previous research suggesting more-or-less complete cover of the landscape by the Scandinavian Ice Sheet at the Last Glacial Maximum (Brook et al., 1996; Goehring et al., 2008; Hughes et al., 2016; Mangerud et al., 2011; Stroeven et al., 2016). All the bedrock samples from Breitinden are likely to have been covered by an ice sheet that was cold-based (see Kleman et al., 2008; Kleman and Hättestrand, 1999). Lack of erosion would account for relatively high levels of inherited ^{10}Be in the two samples from Breitinden that we have interpreted as anomalously old (cf. Briner et al., 2014b; McMartin et al., 2025). The alternative scenario, that Breitinden was a nunatak at the Last Glacial Maximum, that the two relatively old ^{10}Be ages reflect this, and that the single sample with an anomalously young age of ~20 ka reflects enhanced erosion, is considered less likely as it is not supported by the ^{26}Al/^{10}Be ratios from samples BREI-01 and BREI-02 (see Supplemental Table S3).

The ^{10}Be exposure age of the glacially-scoured bedrock surface at just over 1200 m a.s.l. from Skarfjelldalen suggests that deglaciation of areas of the landscape above this elevation occurred by ~14.5 ka (see Figure 10). This is consistent with known rates of lowering of the Scandinavian Ice Sheet (e.g. Goehring et al., 2008; Mangerud et al., 2016, 2019; Regnéll et al., 2022; Stroeven et al., 2016), which in turn suggest that the whole of the Alnesdalen drainage basin was deglaciated before the end of the Bølling-Allerød Interstadial (i.e. by ~13.5 ka). Taking account of the external uncertainties ($\pm 2\sigma$) associated with the mean corrected age of 12.4 ($\pm$1.5) ka, the ^{10}Be age of the Alnesreset samples at an elevation of about 885 m a.s.l. are consistent with this conclusion.

Based on the ^{10}Be ages from the West and East Alnesdalen ice-marginal moraines, local glaciers re-formed and the Scandinavian Ice Sheet re-advanced in the Younger Dryas Stadial. Local glaciers from Finnan advanced from the west as far as mid Alnesdalen while the Scandinavian Ice Sheet re-advanced into upper Alnesdalen from the east. These limits are re-enforced and extended to other parts of the drainage basin, by SHD ages. Particularly important SHD-dated limits to the local glacier that occupied lower Alnesdalen include the moraine ridge to the east of Alnesreset, which indicates that ice did not flow over the col into Valldalen, and the lateral moraines on the valley side near Strupen, which indicate the upper limit of the ice flowing from the South Finnan palaeoglacier towards the mouth of the basin near Stigfossen.

In upper Skarfjelldalen, Younger Dryas ice limits are represented by three sets of moraines, none of which has been dated by ^{10}Be. Two of these relate to small, local palaeocirque glaciers and are dated by SHD, on the north and south side of the valley, respectively. The third set is undated and is inferred from its position to have been deposited by the Younger Dryas Ice Sheet, the edge of which flowed west into the Alnesdalen basin by overtopping the lowest section of the trough end of Skarfjelldalen (see Figure 3). This moraine set is related to a series of moraine ridges that lie outside the Alnesdalen basin, south of the East Alnesdalen moraine at Børtjønna, which are interpreted as representing short halts of the retreating ice sheet.

Precise determination of the timing of the Younger Dryas glacier maximum in Alnesdalen has not been possible. This is likely to have varied somewhat depending on glacier type and location. In the light of proxy evidence from elsewhere in western Norway and offshore, it may have occurred towards the end of the approximately 1200-year duration of the Younger Dryas Stadial. According to Gulliksen et al. (1998) and Bondevik and Mangerud (2002), radiocarbon dating indicates a very late maximum was attained close to the end of the Younger Dryas both at Kråkenes and near Bergen in western Norway, while Bakke et al. (2009) linked this to rapid oceanic and atmospheric changes (see also Mangerud et al., 2023; Naughton et al., 2023b). A large number of ^{10}Be ages obtained recently from moraine ridges in Valldalen suggest maxima between 11.4 $\pm$ 0.2 and 12.3 $\pm$ 0.2 ka ($\pm 1\sigma$; Linge, unpublished).

Substantial climatic fluctuations at the end of the generally cold Younger Dryas Stadial could account for the presence of at least two separate but closely-spaced moraine ridges at several locations in Alnesdalen, the ages of which are too close to be differentiated using either ^{10}Be or SHD. Although cold-based glacier ice must have been common during the coldest climatic fluctuations of the Younger Dryas when permafrost conditions existed down to sea level (Blikra and Longva, 1995; Blikra and Nemec, 1998; Mangerud, 1987), warm-based ice is likely to have occurred beneath active glacier margins during warmer climatic fluctuations and at the end of the stadial when the distinct moraine ridges were deposited (cf. Lane et al., 2020; Matthews et al., 2024).

The ^{10}Be age of 10.8 $\pm$ 1.4 ka for the Finnan moraine, which lies inside Younger Dryas glacial limits and outside 'Little Ice Age' glacial limits, is the sole exposure-age evidence from Alnesdalen for glacial variations in the Early Holocene. This appears to relate to glacial expansion during the Erdalen Event (~10.2 to 9.7 ka), which interrupted the rapid retreat of glaciers in response to Early Holocene climatic warming and produced moraines up to about 1.0 km beyond the Little Ice Age moraine belt elsewhere in southern Norway (Dahl et al., 2002; Matthews et al., 2008; Shakesby et al., 2020). However, the statistical uncertainty is such that an earlier event associated with the Younger Dryas/Holocene transition, such as the Preboreal Oscillation, cannot be ruled out (cf. Lane et al., 2020; Matthews et al., 2024).

The absence of any evidence relating to the extent of glaciers in the Alnesdalen basin later in the Early Holocene and throughout the Mid-Holocene is attributed to their likely absence or very small size during the warmest and driest part of the Holocene (cf. Eldevik et al., 2014; Lilleøren et al., 2012; Mauri et al., 2015; Paus and Haugland, 2017; Wanner et al., 2008). In common with other areas of southern Norway, the glaciers throughout this period of time must have been smaller than they were to become during the Late-Holocene (see Nesje and Matthews, 2024).

'Little Ice Age' moraines occur in front of the cirque glaciers that exist today in the Alnesdalen basin where they provide the only local evidence of glacier variations in the Late-Holocene. Our Schmidt hammer *R*-values and SHD ages are compatible with more precise observational, documentary and lichenometric dating evidence from elsewhere in southern Norway for the deposition of 'Little Ice Age' moraines between the mid 18th century and today (see Nesje and Matthews, 2024). At their 'Little Ice Age' maximum, the glaciers in southern Norway were larger than at any time since the Early Holocene. There can be little doubt, however, that older Late-Holocene (neoglacial) century- to millennial-scale glacier expansion episodes occurred within the Alnesdalen basin but that the glaciers failed to exceed their maximum 'Little Ice Age' dimensions.

Periglacial landscape development

The exposure ages of the different types of landforms provide evidence that the Alnesdalen basin was affected by at least five phases of periglacial landscape development during the Late Glacial and Holocene. Each phase can be seen as a response to environmental changes, including interactions between climate, glacier extent and Earth-surface processes. At different times

and in different parts of the basin, seasonal-frost and permafrost climates, cold-based and warm-based glaciers, and various geomorphological processes of weathering, erosion, transport and deposition were involved.

Late Glacial paraglacial phase of maximum activity (14.6–12.9 ka). In areas of the landscape in upper Alnesdalen and Skarfjelldalen, which were deglaciated during the Bølling-Allerød Interstadial, most landforms started to develop in a paraglacial environment. A paraglacial environment, in which erosion and sedimentation by non-glacial geomorphological processes are directly conditioned by glaciation (Ballantyne, 2002; Church and Ryder, 1972), was effective here immediately following wastage of the Scandinavian Ice Sheet. The subsequent reduction in activity levels and stabilisation of surfaces occurred at rates dependent on specific processes of erosion and deposition. Large rock-slope failures, talus slopes, pronival ramparts, large-scale patterned ground, boulder fields and boulder pavements all fall into this category.

The rock-slope failures that occurred during the Late Glacial paraglacial phase are synchronous depositional surfaces and their exposure ages are therefore relatively easy to interpret. They must have been triggered by one or more paraglacial rock-slope destabilising processes, including ice-sheet thinning, glacial debutressing, hydrostatic pressure variations beneath the ice sheet, glacio-isostatic seismic shock, and seismic triggering from the failure of very large rock avalanches in neighbouring Romsdalen, all of which have been considered important in the Norwegian context (Böhme et al., 2015; Curry, 2021; Henderson and Saintot, 2011; Hermanns et al., 2017; Hilger et al., 2018; Nesje and Matthews, 2024).

Talus slopes and pronival ramparts are associated primarily with the rockfall process driven by the piecemeal release of rock particles from steep rock faces (Ballantyne, 2018; Luckman, 2013; Shakesby, 1997; Statham, 1976). Although the diachronous surfaces of these landforms show clear evidence of later activity, the greater part by volume of the material comprising both the talus slopes and the pronival ramparts must have accumulated prior to the Holocene. If this were not the case, the exposure ages from these features would have been much younger. The contribution of rockfall material from unstable rock-slopes immediately following deglaciation is likely to have been increasingly supplemented by frost weathering (freeze-thaw) processes as paraglacial effects declined and the thermal climate cooled towards the end of the interstadial (cf. Draebing et al., 2025).

Rapid development of large-scale sorted circles by frost sorting shortly after deglaciation in water-saturated till is in accord with formation in a deep active layer associated with seasonal frost (Ballantyne, 2018). Water-saturation would have been characteristic of low-gradient sites as ice-rich sediments thawed near the margin of the downwasting ice sheet. Formation may have been extremely rapid, as demonstrated by their development at ice-marginal sites on glacier forelands in Jotunheimen (Ballantyne and Matthews, 1982; Haugland, 2004, 2006). This argument is strengthened, moreover, by our observation of large-scale sorted circles on the rock-slope failure at site 20. However, an alternative hypothesis, that areas of large-scale patterned ground are relict features that formed much earlier under a permafrost regime (cf. Kessler et al., 2001; Winkler et al., 2016) and survived beneath one or more cold-based ice sheets (cf. Kleman et al., 2008; Nesje and Matthews, 2024) cannot be completely ruled out.

Small areas of boulder fields occur on valley floors within or close to the extensive areas of sorted circles with which they seem to be related. They appear to have developed at the same time as the sorted circles in areas of till from which the fines were removed by groundwater flow, thus rendering frost sorting ineffective. Local conditions for their formation would have been particularly suitable at and near site 56 where the gradient of the valley floor is clearly steeper than in the upstream area of sorted circles, which has a near zero gradient (see Figure 3).

Boulder pavements are best developed in upper Alnesdalen along the shoreline of the shallow lake at 1009 m a.s.l. (see Figure 8c) and along the course of the ephemeral stream downstream of Børtjørna (1069 m). They were also observed in front of semi-permanent snowbeds. The range of SHD ages obtained from these landforms is compatible with the onset of formation immediately after deglaciation, followed by later disturbance. Fines are likely to have been removed from the surface layers of till by shore-washing along the lake shoreline, and by overland flow and throughflow elsewhere. The characteristic pavement effect would have developed over time by a combination of the weight of overlying snow and small incremental horizontal movements of the boulders induced by the freezing and thawing of interstitial ice (cf. Davies et al., 1990; Matthews et al., 1986b).

Younger Dryas permafrost phase (~12.9–11.7 ka). Environmental changes associated with the Younger Dryas Stadial included substantially lower atmospheric and ground temperatures, and widespread permafrost aggradation down to sea level (Blikra and Longva, 1995; Carlson, 2013; Isarin, 1997). The periglacial landscape response to these changes is difficult to determine in Alnesdalen because of the short duration of the stadial, attainable levels of dating precision, and the occurrence of diachronous surfaces affected by later activity. Nevertheless, inferences can be made about relative levels of activity associated with several periglacial landform types.

Some rock-slope failures may have occurred within the Younger Dryas in areas of the basin not covered by glacier ice, possibly as a result of progressive failure. It is likely, however, that most potential failure planes located within bedrock cliffs would have been stabilised by permafrost aggradation at this time (cf. Hilger et al., 2021).

The ages of all four sites on the possible rock glacier are consistent with permafrost aggradation within rock-slope failure deposits leading to the development of interstitial ice, permafrost creep, melt-out features and surface flow structures. However, as discussed in detail by Wilson et al. (2020), the morphological features of this landform supposedly indicative of the presence of permafrost and rock-glacier flow are weakly developed and can result from the more rapid motion associated with rock-slope failures without recourse to the former presence of interstitial ice.

Frost weathering processes responsible for rockfall activity associated with talus slopes and pronival ramparts are likely to have become more effective during the Younger Dryas, as deduced by Blikra and Nemec (1998) from thick, angular open-work boulder deposits at sea-level in neighbouring coastal areas. Under a permafrost regime, frost shattering would have occurred in the bedrock cliffs during autumn freeze-back with subsequent release of rockfall material during spring thaw.

Four out of the five SHD ages from patterned ground sites are consistent with the continuance of frost-sorting processes during the Younger Dryas. Freezing and thawing is likely to have occurred within the active layer above permafrost at this time. By the end of the stadial, however, it is likely that boulder sorting had effectively ceased and most boulders were firmly wedged within the gutters, producing stabilised landforms before the onset of the Holocene.

Three of the four SHD ages from boulder pavements sites are consistent with pavement development continuing during the Younger Dryas. The occurrence of split boulders at these sites bear witness to the likely occurrence of post-depositional frost shattering, at least some of which is likely to have taken place in the active layer during the Younger Dryas.

Early Holocene paraglacial and paraperiglacial phase (~11.7–9.7 ka). Rapid climatic warming and glacier retreat at the start of the Holocene led to a brief paraglacial phase that affected areas of the landscape previously occupied by glaciers in the Younger Dryas Stadial. However, this phase may have been shorter than indicated by our choice of the end of the Erdalen Event as its termination. At the same time, areas of the landscape not occupied by glaciers would have been characterised by permafrost degradation during the transition from a permafrost to a seasonal-frost environment. For these areas, the resulting landforms can be aptly described as paraperiglacial, a term recently used to describe periglacial processes conditioned by the previous existence of permafrost (cf. Mercier, 2008; Scapozza, 2016).

The clearest example of enhanced paraglacial and paraperiglacial activity at this time from this study is the deposition of the alluvial fan (site 59) with an SHD age of 12.47 ± 1.15 ka. This fan, situated alongside the stream currently draining from Bispevatnet, contains large boulders that must have been eroded from the lateral moraines and valley-side till previously deposited upslope in the Younger Dryas and affected by permafrost degradation at the beginning of the Holocene. Discharges and debris content of the river at this time were most likely sufficiently high to constitute debris floods, as inferred for similar relict alluvial fans in the Jotunheimen (McEwen et al., 2020) and Jostedalsbreen areas of southern Norway (Matthews et al., 2020a). There is no evidence of further development of this fan later in the Holocene, unlike the exposure-age dating results from some fans elsewhere with diachronous surfaces (e.g. Dieleman et al., 2025; Walk, 2026).

Although no other landforms in the Alnesdalen basin can be attributed with certainty to this Early Holocene phase, many that were first activated in the Late Glacial paraglacial phase (such as talus slopes and pronival ramparts) are likely to have continued their activity at this time. Furthermore, Carlson et al. (1983) considered that much of the glacially-scoured bedrock that occurs in lower Alnesdalen was water-washed and stripped of overlying sediment during deglacierisation at the end of the Younger Dryas.

Early- to Mid-Holocene phase of minimum activity (~9.7–4.2 ka). With the exception of the three small rock-slope failures near Alnesreset (sites 41, 42 and 48), our study has yielded little evidence of geomorphological activity during this phase, which experienced a generally warm and dry climate and when glaciers were absent from the Alnesdalen basin for most of the time. We tentatively attribute the small rock-slope failures near Alnesreset to the degradation of residual permafrost that could have survived from the previous cold phase and/or variations in hydrostatic pressure (cf. Hilger et al., 2021; Matthews et al., 2018).

Low levels of some other types of periglacial processes doubtless continued in an environment characterised by seasonal frost with relatively shallow frost penetration, reduced summer moisture availability, little colluvial activity and an enhanced vegetation cover. As explained above, the SHD ages derived from the diachronous surfaces of pronival ramparts, talus slopes and snow-avalanche fans, which at first sight might be misinterpreted as indicating the formation of landforms in the Mid-Holocene, most likely reflect the occurrence of the relatively small numbers of surface boulders that were deposited both earlier and later in the Holocene. With a few exceptions, a generally stable landscape in Alnesdalen during the Mid-Holocene is in accord with relatively low levels of periglacial activity across Scandinavia at this time (see Matthews and Nesje, 2022).

Late-Holocene low-activity phase (~4.2–0 ka). Late-Holocene climatic deterioration and neoglaciation led to an appreciable increase in periglacial activity associated with talus slopes, pronival ramparts and snow-avalanche fans. However, the SHD ages from these and similar landforms elsewhere in southern Norway (Matthews et al., 2020b; Matthews and Mourne, 2025; Matthews and Wilson, 2015) demonstrate limited activity relative to the major changes in the landscape that occurred in the earlier paraglacial phases.

The addition of rockfall material to talus slopes and pronival ramparts probably reached its Late-Holocene peak in the 'Little Ice Age' (McCarroll et al., 1998, 2001) and continued at a reduced rate to the present day. Snow-avalanche frequency appears to have been higher in the Late-Holocene than earlier in the Holocene (Nesje et al., 2007; Vasskog et al., 2011) and may also have peaked in the 'Little Ice Age', which was a response to an increase in winter snowfall as well as lower summer temperature (Nesje et al., 2008). Large snow-avalanche events are likely to have occurred in southern Norway throughout the Holocene with a recurrence interval of between ~15 and 150 years (Aa et al., 2022; Decaulne et al., 2014; Nesje and Matthews, 2024; Vasskog et al., 2011).

Glaciofluvial activity since the 'Little Ice Age' is evidenced by our SHD ages on currently active alluvial fans downstream of the West Finnan Glacier, which are essentially modern. Alluvial deposits also exist on the Alnesdalen valley floor, both upstream and downstream of Alnesvatnet, but they exhibit insufficient surface boulders for SHD. We assume, based on southern Norwegian flood records (Bøe et al., 2006; Engeland et al., 2020; Hardeng et al., 2024; Støren et al., 2010, 2012), that fluvial deposition and reworking were more active in the Late-Holocene than at any other time in the Holocene.

Finally, several observations from within the Alnesdalen catchment attest to the presence of Late-Holocene colluvial activity of various types. First, it has already been noted that unweathered boulders and angular shards of rock are scattered across the surface of many of the talus slopes, pronival ramparts and snow-avalanche fans. These rock particles can sometimes be seen perched on other boulders and even balanced on living vegetation beyond the distal limits of these landforms. Second, recent erosion by snow-avalanches at site 88 has been sufficiently potent to reduce a well-weathered bedrock outcrop to a smooth, unweathered one of apparent zero SHD age. Third, parallel levées on talus slopes and snow-avalanche fans provide evidence of reworking by debris flows (see, e.g. Figure 7c). Fourth, some sorted circles exhibit evidence of centres disturbed by shallow cryoturbation but this secondary activity is unrelated to the original frost-sorting processes that produced the long-stabilised boulder-filled relict gutters. Fifth, on the glacier foreland of the West Finnan Glacier, the steep, unvegetated proximal slope of the northern lateral 'Little Ice Age' moraine (Figures 4a and 6a) appears to have remained unstable since deposition. Shallow slumping and gullying of unconsolidated till slopes at this location represent neoparaglacial processes that are conditioned by glacial retreat since the 'Little Ice Age' maximum (cf. Ballantyne and Benn, 1994; Lukas et al., 2012; Tonkin, 2023).

With the exception of the special circumstances on the glacier foreland, periglacial landscape development was therefore severely limited during the Late-Holocene phase. Furthermore, with the possible exception of gelifluction continuing beneath the surface of solifluction lobes, frost-related periglacial processes were largely ineffective and remain so at present.

Methodological evaluation

We have demonstrated an approach to understanding the nature and development of glacial and periglacial landscapes over Late Glacial and Holocene timescales. The approach focussed on dating an extensive array of landforms present in the Alnesdalen drainage basin. The landscape was thereby conceptualised as a

mosaic of individual elements or geomorphosites (*sensu* Reynard, 2005; see also Reynard et al., 2009). Numerical exposure-age estimates for each site enabled the reconstruction of glacial history and established the timing of the paraglacial, periglacial and paraperiglacial response to the major environmental changes of the last ~15,000 years.

Many excellent geomorphological maps show the distribution and interrelationships of glacial and periglacial landforms in alpine landscapes. However, the temporal aspects of the landscape mosaic are much more difficult to assess than the spatial aspects, and a complete numerical-age chronology of a similar geomorphological landscape has not been attempted before. In relation to individual landform types, such as moraines, rock glaciers, alluvial fans and rock-slope failures, ^{10}Be dating provides a way forward, but cost currently prohibits dating the complete landscape mosaic using this technique. The potential of SHD has been demonstrated, in principle, by Santos-González et al. (2024). They used Schmidt hammer *R*-values for relative-age dating of moraines, erratics, polished bedrock, rock glaciers, talus slopes and blockfields in several landscapes of the Cantabrian Mountains and Montes de Leon of northwestern Spain. Their study involved three different lithologies across five massifs but, without adequate control surfaces of known age, they were unable to carry out age-calibration and produce numerical SHD age estimates.

Our approach was made possible by the combined application of ^{10}Be dating and SHD. The former technique provided numerical age estimates from a relatively small number of sites on mainly glacial landforms, whereas the latter enabled a larger number of calibrated-age estimates to be obtained from a diverse array of landforms using the local ^{10}Be ages as calibration data. Direct comparisons between the age estimates from the two techniques are possible for seven landforms where both ^{10}Be and SHD ages are available (Figure 13). The age estimates are in generally good agreement and, according to the overlapping uncertainties, there is no significant difference in age between six of the seven landforms. The results from the two techniques are seriously out of line only in the case of the Finnan moraine (site 35) where we argue that the SHD age is anomalous. However, as the local ^{10}Be ages were used for SHD age calibration, the age estimates from the two techniques are not independent in this study. Comparative accuracy may also be questioned on the basis of the small number of samples used for ^{10}Be dating and the preference for relatively large boulders, which are not necessarily representative and potentially bear a high risk of inheritance (Hilger et al., 2019).

^{10}Be dating and SHD have common limitations, related to those of exposure-age dating in general, and technique-specific limitations. Common limitations include those of surface-age determination in general, which, by definition, refer to the landform surface only and therefore may differ from the age of the subsurface if the landform developed over a long period of time or involved more than one event. Landform-surface age may therefore bear little or no relation to the early stages of landform development or landform age (the latter defined as the time elapsed since the onset of landform development). Both exposure-age techniques can also be subject to interpretive problems associated with post-depositional or post-erosional events that may affect surface ages.

Another important limitation that affects both techniques is their similar millennial-scale level of achievable age resolution. Age resolution is reflected in the statistical uncertainties ($\pm 2\sigma$) attached to each age estimate which, for exposure ages from the Late Glacial and Holocene in this study, are 1.1–1.7 ka for SHD ages and 1.5–2.5 for ^{10}Be ages. This creates ambiguity when trying to interpret relatively brief events in glacier history or short phases in periglacial landscape development (such as those associated with the ~1.2 ka duration of the Younger Dryas or the ~0.6 ka duration of the 'Little Ice Age'). Nevertheless, both techniques effectively distinguish major differences in exposure age across the landscape and provide a window on the major environmental changes affecting the landscape during the Late Glacial and Holocene.

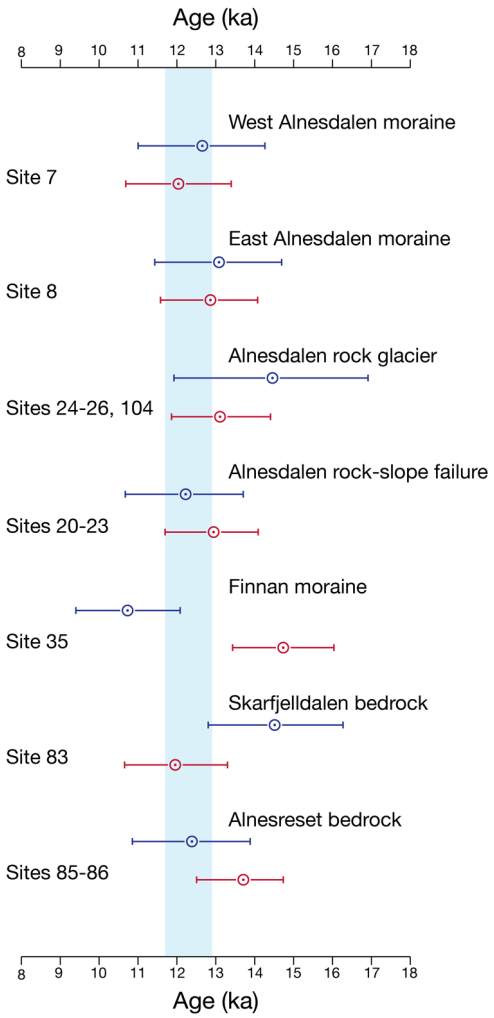

Figure 13. ^{10}Be and SHD ages for sites where both techniques were used and direct comparison is possible. ^{10}Be ages (blue) are mean corrected ages as in Table 2 with 2σ external uncertainties. SHD ages (red) are mean ages with 95% confidence intervals from Table 4. The vertical light blue band spans the Younger Dryas Stadial.

Important specific limitations of ^{10}Be ages in the present context relate to possible dating inaccuracies associated with our choice of on-line calculator, the global ^{10}Be production rate and our inclusion of three environmental corrections for land uplift, snow depth and erosion. Inheritance (in this case, of pre-exposure ^{10}Be) also proved important in accounting for some anomalously old ^{10}Be ages, and some anomalously young ages can be explained by post-depositional boulder disturbances. Use of realistic 2σ external statistical uncertainties (rather than the usual practice of 1σ when discussing ^{10}Be ages) contributes a partial but ultimately inadequate solution to the existence of these limitations.

Inheritance (in this case, of pre-weathered surfaces) may also explain some anomalously old SHD ages, while locally enhanced weathering (leading to the exposure of less weathered rock) may account for some anomalously young SHD ages. Our use of two age-calibration equations has certainly reduced the extent of any effect on SHD ages of initial differences in roughness between surfaces. However, high lithological variability in the local

gneissic rocks remains the most important source of inaccuracy in our SHD ages from Alnesdalen.

Variations in mineralogy, grain size and banding were often difficult to recognise and control during field sampling for SHD. Although within-site variability is adequately accounted for by the sample size of 200 *R*-value impacts per site used in this study, it is more difficult to take account of between-site variability. Our modification to the two-point SHD age-calibration method, which approximately doubles the width of previously used (unmodified) confidence intervals, takes some account of between-site variability in *R*-values, but provides only a partial solution to the problems posed by high lithological variability. This is clear from the extent of the variability in *R*-values revealed in this study and also in the large number of independently-dated gneissic surfaces associated with large rock-slope failures located in the wider southern Norwegian gneiss region beyond the Alnesdalen drainage basin (Pytten, 2024).

Conclusions

This case study demonstrates a viable exposure-age dating approach to understanding glacial and periglacial landscapes where exposed boulder and bedrock surfaces are abundant, and where other dating techniques (e.g. radiocarbon dating) and approaches (e.g. use of stratigraphic relationships) may not be applicable. Combined and integrated use of cosmogenic ^{10}Be and Schmidt-hammer (SHD) dating of landform surfaces has revealed a palimpsest landscape in the Alnesdalen drainage basin consisting of a mosaic of largely relict landscape elements with a wide range of surface ages from the Late Glacial and Holocene. The achievement of millennial-scale age resolution by both techniques allows detection of large differences in age related to the major environmental changes that have affected the landscape. Several methodological limitations of exposure-age dating were identified during this study. The ^{10}Be exposure ages were significantly affected by the choice of on-line calculator, ^{10}Be production rate and the environmental corrections for land uplift, snow shielding and surface erosion. In relation to SHD, high lithological variation in the local gneissic rocks was found to be particularly important. Inheritance affected both techniques in different ways.

The extent and history of the glaciers has been reconstructed based mainly on ^{10}Be ages from glacially-transported boulders associated with ice-marginal moraines and valley-floor glacially-scoured bedrock. Downwasting of the Scandinavian Ice Sheet after the Last Glacial Maximum led to exposure of the highest summit in the basin (Bretinden, 1797 m a.s.l,.) at around ~20 ka. Deglaciation of the valley-side slopes and valley floors (down to ~700 m a.s.l.) occurred during the Bölling-Allerød Interstadial (14.6–12.9 ka) when extensive areas of till were deposited in upper Alnesdalen and upper Skarfjelldalen. In the Younger Dryas Stadial (12.9–11.7 ka), re-advance of the ice sheet from the east reached the upper end of Alnesdalen, while local glaciers advanced from Finnan into lower Alnesdalen and in Skarfjelldalen. Extensive areas of glacially-scoured bedrock on the valley floor of lower Alnesdalen (~700 m a.s.l.) were exposed during the Younger Dryas/Holocene transition following rapid retreat of local glaciers and climate amelioration. Moraine ridges of Early- and Late-Holocene age occur in front of the present-day east-facing South Finnan cirque glacier. These are attributed to glacier advances during the 'Erdalen Event' (~10.2–9.7 ka) and the 'Little Ice Age' (~0.5–0 ka). At its maximum extent during the 'Erdalen Event', this glacier advanced $<$500 m beyond its 'Little Ice Age' limit. In the tributary valley of Skarfjelldalen, small north-facing cirque glaciers almost reached their Younger Dryas dimensions in the 'Little Ice Age'

Five phases of periglacial landscape development are recognised based mainly on SHD age estimates from the wide variety of depositional landforms occurring in the Alnesdalen basin. These phases are: the *Late Glacial paraglacial phase of maximum activity, which occurred* during the Bölling-Allerød Interstadial (14.6 –12.9 ka); the *Younger Dryas permafrost phase* (~12.9–11.7 ka); the *Early Holocene paraglacial and paraperiglacial phase* (~11.7–9.7 ka); the *Early- to Mid-Holocene phase of minimum activity* (~9.7–4.2 ka); and the *Late-Holocene low-activity phase* (~4.2–0 ka). The largest rock-slope failures were activated and talus slopes, pronival ramparts and snow-avalanche fans started to develop rapidly during the Late Glacial paraglacial phase. Extensive areas of large-scale patterned ground on extremely low-gradient areas of valley floors in upper Alnesdalen and Skarfjelldalen appear to have formed rapidly in a deep active layer in water-saturated till immediately after deglaciation and then became relict (possibly after further limited development during the Younger Dryas). A similar pattern of development is evident for smaller areas of allochthonous boulder fields on valley floors where the gradient was slightly steeper and/or the till contained less fine sediment. Boulder pavement development occurred over a relatively long period of time during the Late Glacial and Holocene..

Whereas the glacier variations of the last ~15,000 years in the Alnesdalen drainage basin have been directly driven by climatic fluctuations, the periglacial landscape response to environmental change over this time interval has been dominated by paraglacial processes. During the Younger Dryas paraglacial phase, permafrost aggradation may have activated a short-lived rock glacier in the coarse debris deposit of a rock-slope failure in upper Alnesdalen. Permafrost degradation is likely to have been effective in the development of an alluvial fan during the Early Holocene paraglacial and paraperiglacial phase when relatively small-scale rock-slope failures may also have been triggered. Low levels of periglacial activity occurred under the seasonal-frost regime of the late Early and Mid-Holocene. As climate became cooler and wetter in the Late-Holocene, modest glacier growth led to the development of glaciofluvial alluvial fans while minor additions of coarse debris originating from rockfall were made to talus slopes, pronival ramparts and snow-avalanche fans.

Our final, overall conclusion is that surface exposure-age dating techniques have considerable untapped potential in glacial and periglacial landscapes and beyond. In particular, they can reveal spatial and temporal variation in exposure-ages between the many different kinds of landforms produced by different processes under changing environmental conditions. An understanding of surface exposure-age variations within the landscape thereby provides a unique approach to reconstructing geomorphological change, its environmental drivers, and its dynamics.

Acknowledgements

Cosmogenic exposure dating for the project was made possible by a Research Collaboration Agreement between University of Bergen (HL) and the Jotunheimen Research Trust (JAM). Fieldwork was conducted during the Jotunheimen Research Expeditions of 2013–2023. We thank John Inge Svendsen, Anna Hughes and Øystein Lohne for collecting and donating the TROLL sample, Anne-Sofie Ertesvåg and Atle Nesje for calibrating radiocarbon ages, and Judith Vestre for doing the initial assessment of Al/Be-data from Breitinden. We acknowledge the assistance of senior engineer Lars Evje, for preparing AMS targets from rock samples. We are also grateful to Anna Ratcliffe, who prepared most of the figures for publication, to Anders Gjerde, for logistical support while we were based at Gjerde Camping, Valldalen, and to Vigdis Linge for accommodation and support over the years. The comments of Stefan Winkler and an anonymous reviewer improved the manuscript. This paper represents Jotunheimen Research Expeditions, Contribution No. 232 (see http://jotunheimenresearch.wixsite.com/home).

Author contributions

John A. Matthews: Conceptualisation; Formal analysis; Investigation; Methodology; Writing – original draft.
Henriette Linge: Formal analysis; Investigation; Methodology; Writing – review & editing.
Peter Wilson: Investigation; Writing – review & editing.
Richard W Mourne: Investigation; Writing – review & editing.
Paula Snook: Investigation; Writing – review & editing.
Jennifer L. Hill: Investigation; Writing – review & editing.
Jesper Olsen: Formal analysis.

Funding

The authors received no financial support for the research, authorship, and/or publication of this article.

ORCID iDs

John A Matthews https://orcid.org/0000-0002-2610-863X
Henriette Linge https://orcid.org/0000-0002-6069-5348

Supplemental material

Supplemental material for this article is available online.

References

Aa AR, Bondevik S and Sønstegaard E (2022) Holocene debris flows and snow avalanches in Anestølsdalen, Western Norway – Recorded from lake deposits and colluvial fans. *Norwegian Journal of Geology* 102: 202207.

Altınay O and Sarıkaya MA (2025) First calibration site for Schmidt hammer exposure-age dating (SHD) in Türkiye and an experimental approach on ultramafic rocks. *Mediterranean Geoscience Reviews* 7: 545–560.

Andreassen LM and Winsvold SH (eds)(2012) *Inventory of Norwegian Glaciers*. Oslo: Norwegian Water Resources and Energy Directorate, Rapport (34–2012).

André M (2002) Rates of postglacial rock weathering on glacially scoured outcrops (Abisko–Riksgränsen area, 68° N). *Geografiska Annaler Series A Physical Geography* 84: 139–150.

Bakke J, Lie Ø, Heegaard E et al. (2009) Rapid oceanic and atmospheric changes during the Younger Dryas cold period. *Nature Geoscience* 2: 202–205.

Balco G (2011) Contributions and unrealized potential contributions of cosmogenic-nuclide exposure dating to glacier chronology, 1990–2010. *Quaternary Science Reviews* 30: 3–27.

Balco G (2020) Glacier change and paleoclimate applications of cosmogenic-nuclide exposure dating. *Annual Review of Earth and Planetary Sciences* 48: 21–48.

Balco G, Stone JO, Lifton NA et al. (2008) A complete and easily accessible means of calculating surface exposure ages or erosion rates from ^{10}Be and ^{26}Al measurements. *Quaternary Geochronology* 3: 174–195.

Ballantyne CK (2002) Paraglacial geomorphology. *Quaternary Science Reviews* 21: 1935–2017.

Ballantyne CK (2018) *Periglacial Geomorphology*. Chichester: Wiley-Blackwell.

Ballantyne CK and Benn DI (1994) Paraglacial slope adjustment and resedimentation following recent glacier retreat, Fabergstolsdalen, Norway. *Arctic and Alpine Research* 26: 255–269.

Ballantyne CK and Matthews JA (1982) The development of sorted circles on recently deglaciated terrain, Jotunheimen, Norway. *Arctic and Alpine Research* 14: 341–354.

Blikra LH and Longva O (1995) Frost-shattered debris facies of Younger Dryas age in the coastal sedimentary successions in Western Norway: Palaeoenvironmental implications. *Palaeogeography Palaeoclimatology Palaeoecology* 118: 89–110.

Blikra LH and Nemec W (1998) Postglacial colluvium in Western Norway: Depositional processes, facies and palaeoclimatic record. *Sedimentology* 45: 909–959.

Bøe AG, Dahl SO, Lie Ø et al. (2006) Holocene river floods in the upper Glomma catchment, Southern Norway: A high-resolution multiproxy record from lacustrine sediments. *Holocene* 16: 445–455.

Böhme M, Oppikofer T, Longva O et al. (2015) Analyses of past and present rock slope instabilities in a Fjord valley: Implications for hazard estimations. *Geomorphology* 248: 464–474.

Bondevik S and Mangerud J (2002) A calendar age estimate of a very late Younger Dryas ice sheet maximum in Western Norway. *Quaternary Science Reviews* 21: 1661–1676.

Borchers B, Marrero S, Balco G et al. (2016) Geologic calibration of spallation production rates in the CRONUS-earth project. *Quaternary Geochronology* 31: 188–198.

Boulton GS (1978) Boulder shapes and grain-size distributions of debris as indicators of transport paths through a glacier and till genesis. *Sedimentology* 25: 773–799.

Briner JP, Lifton NA, Miller GH et al. (2014a) Using in situ cosmogenic 10Be, 14C, and 26Al to decipher the history of polythermal ice sheets on Baffin Island, Arctic Canada. *Quaternary Geochronology* 19: 4–13.

Briner JP, Svendsen JI, Mangerud J et al. (2023) Configuration of the Scandinavian ice sheet in Southwestern Norway during the Younger Dryas. *Norwegian Journal of Geology* 103: 202311.

Briner JP, Svendsen JI, Mangerud J et al. (2014b) A ^{10}Be chronology of South-western Scandinavian ice sheet history during the Lateglacial period. *Journal of Quaternary Science* 29: 370–380.

Brook EJ, Nesje A, Lehman SJ et al. (1996) Cosmogenic nuclide exposure ages along a vertical transect in Western Norway: Implications for the height of the Fennoscandian ice sheet. *Geology* 24: 207–210.

Carlson A (2013) The Younger Dryas climate event. In: Elias SA and Mock CJ (eds) *Encyclopedia of Quaternary Science*, vol. 3. Amsterdam: Elsevier, pp.126–134.

Carlson AB, Sollid JL and Torp B (1983) *Valldal. Kvartærgeologi og Geomorfologi 1:50,000, sheet 1319 IV*. Oslo: Geografisk Institutt, Universitetet I Oslo.

Chorley RJ (1969) The drainage basin as the fundamental geomorphic unit. In: Chorley RJ (ed.) *Water, Earth and Man*. London: Methuen, pp.77–99.

Church M and Ryder JM (1972) Paraglacial sedimentation: A consideration of fluvial processes conditioned by glaciation. *Geological Society of America Bulletin* 83: 3059–3072.

Curry AM (2021) Paraglacial rock-slope failure following deglaciation in Western Norway. In: Beylich AA (ed.) *Landscapes and Landforms of Norway*. Cham: Springer Nature, pp.97–130.

Dahl SO, Nesje A, Lie Ø et al. (2002) Timing, equilibrium-line altitudes and climatic implications of two early-Holocene glacier readvances during the Erdalen event at Jostedalsbreen, Western Norway. *Holocene* 12: 17–25.

Dalsegg E and Tønneson JF (2004) Geofysiske Malinger Breitind og Børa, Rauma Commune, Møre og Romsdal. NGU Report 2004-008. Available at: https://www.ngu.no/publikasjon/grofysiske-malinger-breitind-og-bora-rauma-kommune-more-og-romsdal

Davies DA, Berrisford MS and Matthews JA (1990) Boulder-paved river channels: A case study of a fluvio-periglacial landform. *Zeitschrift für Geomorphologie* 34: 213–231.

Decaulne A, Eggertsson Ó, Laute K et al. (2014) A 100-year extreme snow-avalanche record based on tree-ring research in upper Bødalen, inner Nordfjord, Western Norway. *Geomorphology* 218: 3–15.

Dieleman C, Deline P, Ivy Ochs S et al. (2025) Unravelling the evolution of the Frébouge polygenetic cone in Val Ferret (Mont Blanc massif). *Boreas* 1–22. DOI: 10.1111/bor.70042

Draebing D, Pandis GA and Nijland W (2025) Paraglacial and periglacial processes drive headwall erosion in a deglaciating Swiss cirque. *Geomorphology* 482: 109799.

Dunne J, Elmore D and Muzikar P (1999) Scaling factors for the rates of production of cosmogenic nuclides for geometric shielding and attenuation at depth on sloped surfaces. *Geomorphology* 27: 3–11.

Eldevik T, Risebrobakken B, Bjune A et al. (2014) A brief history of climate — The northern seas from the last glacial maximum to global warming. *Quaternary Science Reviews* 106: 225–246.

Engeland K, Aano A, Steffensen I et al. (2020) New flood frequency estimates for the largest river in Norway based on the combination of short and long time series. *Hydrology and Earth System Sciences* 24: 5595–5619.

Etzelmüller B, Berthling I and Sollid JL (2003) Aspects and concepts on the geomorphological significance of Holocene permafrost in Southern Norway. *Geomorphology* 52: 87–104.

Etzelmüller B and Hagen JO (2005) Glacier-permafrost interaction in Arctic and Alpine mountain environments with examples from Southern Norway and Svalbard. In: Harris C and Murton JB (eds) *Cryospheric Systems: Glaciers and Permafrost*, vol. 242. London: Geological Society, pp.11–27, Special Publication.

Fletcher WJ, Sánchez-Goñi MF, Naughton F et al. (2024) Greenlandian stage (Early Holocene, 11.7–8.2 ka). In: Palacios D, Hughes PD, Jomelli V et al. (eds) *European Glacial Landscapes: The Holocene*. Elsevier: Amsterdam, pp.73–87.

Gisnås K, Etzelmüller B, Lussana C et al. (2017) Permafrost map for Norway, Sweden and Finland. *Permafrost and Periglacial Processes* 28: 359–378.

Goehring BM, Brook EJ, Linge H et al. (2008) Beryllium-10 exposure ages of erratic boulders in Southern Norway and implications for the history of the Fennoscandian ice sheet. *Quaternary Science Reviews* 27: 320–336.

Gulliksen S, Birks HH, Possnert G et al. (1998) A calendar age estimate of the Younger Dryas - Holocene boundary at Kråkenes, Western Norway. *Holocene* 8: 249–259.

Hardeng J, Bakke J, Cederstrøm JM et al. (2024) A 7000-year record of extreme flood events reconstructed from a threshold lake in Southern Norway. *Quaternary Science Reviews* 331: 108650.

Haugland JE (2004) Formation of patterned ground and fine-scale soil development within two Late-Holocene glacial chronosequences: Jotunheimen, Norway. *Geomorphology* 61: 287–301.

Haugland JE (2006) Short-term periglacial processes, vegetation succession, and soil development within sorted patterned ground: Jotunheimen, Norway. *Arctic, Antarctic, and Alpine Research* 38: 82–89.

Hedding DW and Sumner PD (2013) Diagnostic criteria for pronival ramparts: Site, morphological and sedimentological characteristics. *Geografiska Annaler, Series A* 95: 315–322.

Henderson IHC and Saintot A (2011) Regional spatial variations in rockslide distribution from structural geology ranking: An example from Storfjorden, Western Norway. In: Jaboyedoff M (ed.) *Slope Tectonics*, Geology Society, vol. 351. London: Special Publications, pp.59–70.

Hermanns RL, Schleier M, Böhme M et al. (2017) Rock avalanche activity in W and S Norway peaks after the retreat of the Scandinavian ice sheet. In: Ikos M, Ilímek M, In V et al. (eds) *Advancing Culture of Living With Landslides, Volume 5: Landslides in Different Environments*. Heidelberg: Heidelberg, pp.331–338.

Hilger P, Gosse JC and Hermanns RL (2019) How significant is inheritance when dating rockslide boulders with terrestrial cosmogenic nuclide dating?—A case study of an historic event. *Landslides* 16: 729–738.

Hilger P, Hermanns RL, Czekirda J et al. (2021) Permafrost as a first order control on long-term rock-slope deformation in (Sub-)Arctic Norway. *Quaternary Science Reviews* 251: 1–21.

Hilger P, Hermanns RL, Gosse JC et al. (2018) Multiple rock-slope failures from Mannen in Romsdal valley, Western Norway, revealed from Quaternary geological mapping and ^{10}Be exposure dating. *Holocene* 28: 1841–1854.

Hughes ALC, Gyllencreutz R, Lohne ØS et al. (2016) The last Eurasian ice sheets – A chronological database and time-slice reconstruction, DATED-1. *Boreas* 45(1): 1–45.

Isarin RFB (1997) Permafrost distribution and temperatures in Europe during the Younger Dryas. *Permafrost and Periglacial Processes* 8: 313–333.

Jones RS, Small D, Cahill N et al. (2019) iceTEA: Tools for plotting and analysing cosmogenic-nuclide surface-exposure data from former ice margins. *Quaternary Geochronology* 51: 72–86.

Karakul H (2017) Investigation of saturation effect on the relationship between compressive strength and Schmidt hammer rebound. *Bulletin of Engineering Geology and the Environment* 76: 1143–1152.

Karakul H (2020) Investigation of the effect of impact direction on Schmidt rebound values by multivariate regression and neuro-fuzzy model. *SN Applied Sciences* 2: 1807.

Kessler MA, Murray AB, Werner BT et al. (2001) A model for sorted circles as self-organized patterns. *Journal of Geophysical Research* 106: 13287–13306.

Khashchevskaya D, Owen LA, Wegmann K et al. (2025) The characteristics and timing of multiphase major landslides along the Blue Ridge escarpment of the Southern Appalachians revealed by combined cosmogenic nuclide dating and Schmidt hammer rebound measurements. *Geomorphology* 485: 109857.

Kleman J and Hättestrand C (1999) Frozen-bed Fennoscandian and Laurentide ice sheets during the last glacial maximum. *Nature* 402: 63–66.

Kleman J, Stroeven AP and Lundqvist J (2008) Patterns of Quaternary ice sheet erosion and deposition in Fennoscandia and a theoretical framework for explanation. *Geomorphology* 97: 73–90.

Lane TP, Paasche Ø, Kvisvik B et al. (2020) Elevation changes of the Fennoscandian ice sheet interior during the last deglaciation. *Geophysical Research Letters* 47: e2929GL088796.

Lifton N, Sato T and Dunai TJ (2014) Scaling in situ cosmogenic nuclide production rates using analytical approximations to atmospheric cosmic-ray fluxes. *Earth and Planetary Science Letters* 386: 149–160.

Lilleøren KS, Etzelmüller B, Schuler TV et al. (2012) The relative age of mountain permafrost — Estimation of Holocene permafrost limits in Norway. *Global and Planetary Change* 92-93: 209–223.

Linge H, Nesje A, Fjellheim SF et al. (2025) Be-10 exposure ages from 25 published and assumed Younger Dryas sites in Norway (59–70º N, 6–30º E). Which calculator, scaling scheme and ^{10}Be production rate to use for surface exposure dating? In: *Poster presentation at the winter meeting of the Geological Society of Norway*, Bergen, 2025. NGF Abstracts and Proceedings 1: 58.

Linge H, Nesje A, Matthews JA et al. (2020) Evidence for rapid paraglacial formation of rock glaciers in Southern Norway from ^{10}Be surface-exposure dating. *Quaternary Research* 97: 55–70.

Longhi A, Morgan D and Guglielmin M (2024) Reconstruction of rock avalanche history in Val Viola, (Upper Valtellina, Italian Central Alps) through ^{10}Be exposure ages, Schmidt hammer R values, and surface roughness. *Landslides* 21: 949–962.

Luckman BH (2013) Talus slopes. In: Elias SA and Mock CJ (eds) *Encyclopedia of Quaternary Science*, vol. 3. Amsterdam: Elsevier, pp.566–573.

Lukas S, Graf A, Coray S et al. (2012) Genesis, stability and preservation potential of large lateral moraines of Alpine valley glaciers – Towards a unifying theory based on Findelengletscher, Switzerland. *Quaternary Science Reviews* 38: 27–48.

Magnin F, Etzelmüller B, Westermann S et al. (2019) Permafrost distribution in steep rock slopes in Norway: Measurements, statistical modelling and implications for geomorphological processes. *Earth Surface Dynamics* 7: 1019–1040.

Makopoulou E, Trombotto Liaudat D and Kuhry P (2025) Glacial and periglacial landforms and their recent dynamics in the Las Veguitas catchment, Cordillera Frontal of the Andes (Argentina). *Frontiers in Earth Science* 13: 1533336.

Mangerud J (1987) The Alleröd/Younger Dryas boundary. In: Berger WH and Labeyrie LD (eds) *Abrupt Climatic Change: Evidence and Implications*, NATO ASI Series (Series C: Mathematical and Physical Sciences), vol. 216. Dordrecht: Springer, pp.163–171.

Mangerud J, Aarseth I, Hughes ALC et al. (2016) A major regrowth of the Scandinavian ice sheet in Western Norway during Allerød-Younger Dryas. *Quaternary Science Reviews* 132: 175–205.

Mangerud J, Gyllencreutz R, Lohne Ø et al. (2011) Glacial history of Norway. In: Ehlers J, Gibbard PL and Hughes PD (eds) *Quaternary Glaciations – Extent and Chronology: A Closer Look*. Amsterdam: Elsevier, pp.279–298.

Mangerud J, Hughes ALC, Johnson MD et al. (2023) The Fennoscandian ice sheet during the Younger Dryas stadial. In: Palacios D, Hughes PD, García-Ruiz JM et al. (eds) *European Glacial Landscapes. The Last Deglaciation*. Amsterdam: Elsevier, pp.437–452.

Mangerud J, Hughes ALC, Sæle TH et al. (2019) Ice-flow patterns and precise timing of ice sheet retreat across a dissected fjord landscape in Western Norway. *Quaternary Science Reviews* 214: 139–163.

Marr P, Winkler S, Dahl SO et al. (2022) Age, origin and palaeoclimatic implications of peri- and paraglacial boulder-dominated landforms in Rondane, South Norway. *Geomorphology* 408: 108251.

Marr P, Winkler S and Löffler J (2019) Schmidt-hammer exposure-age dating (SHD) performed on periglacial and related landforms in Opplendskedalen, Geirangerfjellet, Norway: Implications for mid- and Late-Holocene climate variability. *Holocene* 29: 97–109.

Matthews JA, Harris C and Ballantyne CK (1986a) Studies on a gelifluction lobe, Jotunheimen, Norway: ^{14}C chronology, stratigraphy, sedimentology and palaeoenvironment. *Geografiska Annaler, Series A* 86: 345–360.

Matthews JA, Dawson AG and Shakesby RA (1986b) Lake shoreline development, frost weathering and rock platform erosion in an Alpine periglacial environment. *Boreas* 15: 33–50.

Matthews JA (1987) Regional variation in the composition of neoglacial end moraines, Jotunheimen, Norway: An altitudinal gradient in clast roundness and its possible climatic implications. *Boreas* 16: 173–188.

Matthews JA, Haselberger S, Hill JL et al. (2020b) Snow-avalanche boulder fans in Jotunheimen, Southern Norway: Schmidt-hammer exposure-age dating, geomorphometrics, dynamics and evolution. *Geografiska Annaler Series A* 102: 118–140.

Matthews JA, Linge H, Nesje A et al. (2024) Deglaciation of the highest mountains in Scandinavia at the Younger Dryas–Holocene transition: Evidence from surface exposure-age dating of ice-marginal moraines. *Boreas* 53: 139–163.

Matthews JA and McEwen LJ (2013) High-precision Schmidt-Hammer exposure-age dating of flood berms, Vetlestølsdalen, Alpine Southern Norway: First application and some methodological issues. *Geografiska Annaler, Series A* 95: 185–195.

Matthews JA, McEwen LJ, Owen G et al. (2020a) Holocene alluvial fan evolution, Schmidt-hammer exposure-age dating and paraglacial debris floods in the SE Jostedalsbreen region, Southern Norway. *Boreas* 49: 886–902.

Matthews JA and Mourne RW (2025) Schmidt-hammer exposure-age dating of talus slopes in upper Jostedalen, Southern Norway: Interpreting the age and development of diachronous surfaces. *Holocene* 35: 340–351.

Matthews JA and Nesje A (2022) Scandinavia. In: Oliva M, Nývlt D and Fernández-Fernández JM (eds) *Periglacial Landscapes of Europe*. Cham: Springer Nature Switzerland AG, pp.365–426.

Matthews JA and Owen G (2010) Schmidt hammer exposure-age dating: developing linear age-calibration curves using Holocene bedrock surfaces from the Jotunheimen-Jostedalsbreen regions of Southern Norway. *Boreas* 39: 105–115.

Matthews JA and Owen G (2011) Holocene chemical weathering, surface lowering and rock weakening rates on glacially eroded bedrock surfaces in an alpine periglacial environment, Jotunheimen, Southern Norway. *Permafrost and Periglacial Processes* 22: 279–290.

Matthews JA, Owen G, Winkler S et al. (2016) A rock-surface microweathering index from Schmidt hammer R-values and its preliminary application to some common rock types in Southern Norway. *Catena* 143: 35–44.

Matthews JA, Shakesby RA, Schnabel C et al. (2008) Cosmogenic ^{10}Be and ^{26}Al ages of Holocene moraines in Southern Norway I: Testing the method and confirmation of the date of the Erdalen event (c. 10 ka) at its type-site. *Holocene* 18: 1155–1164.

Matthews JA and Wilson P (2015) Improved Schmidt-hammer exposure ages for active and relict pronival ramparts in Southern Norway, and their palaeoenvironmental implications. *Geomorphology* 246: 7–21.

Matthews JA and Winkler S (2022) Schmidt-hammer exposure-age dating: A review of principles and practice. *Earth-Science Reviews* 230: 104038.

Matthews JA, Winkler S, Wilson P et al. (2018) Small rock-slope failures conditioned by Holocene permafrost degradation: A new approach and conceptual model based on Schmidt-hammer exposure-age dating, Jotunheimen, Southern Norway. *Boreas* 47: 1144–1169.

Mauri A, Davis BAS, Collins PM et al. (2015) The climate of Europe during the Holocene: A gridded pollen-based reconstruction and its multi-proxy evaluation. *Quaternary Science Reviews* 112: 109–127.

McCarroll D, Shakesby RA and Matthews JA (1998) Spatial and temporal patterns of late-Holocene rockfall activity on a Norwegian talus slope: A lichenometric and simulation-modeling approach. *Arctic and Alpine Research* 30: 51–60.

McCarroll D, Shakesby RA and Matthews JA (2001) Enhanced rockfall activity during the little ice age: Further lichenometric evidence from a Norwegian talus. *Permafrost and Periglacial Processes* 12: 157–164.

McEwen LJ, Matthews JA and Owen G (2020) Development of a Holocene glacier-fed composite alluvial fan based on surface

exposure-age dating techniques: The Illåe fan, Jotunheimen, Norway. *Geomorphology* 363: 107200.

McMartin I, Godbout P-M, Tremblay T et al. (2025) Paired terrestrial cosmogenic nuclides support the mapping of relict polythermal terrains under the Keewatin ice divide, Central Mainland Nunavut, Canada. *Quaternary Science Reviews* 366: 109505.

Mercier D (2008) Paraglacial and paraperiglacial landsystems: Concepts, temporal scales and spatial distribution. *Géomorphologie: Relief, Processus and Environment* 14: 223–233.

Naughton F, Sánchez-Goñi MF, Landais A et al. (2023a) The Bölling-Allerød interstadial. In: Palacios D, Hughes PD, García-Ruiz JM et al. (eds) *European Glacial Landscapes: The Last Deglaciation*. Amsterdam: Elsevier, pp.45–50.

Naughton F, Sánchez-Goñi MF, Landais A et al. (2023b) The Younger Dryas stadial. In: Palacios D, Hughes PD, García-Ruiz JM et al. (eds) *European Glacial Landscapes: The Last Deglaciation*. Amsterdam: Elsevier, pp.51–57.

Nesje A (2009) Latest Pleistocene and Holocene alpine glacier fluctuations in Scandinavia. *Quaternary Science Reviews* 28: 2119–2136.

Nesje A, Bakke J, Dahl SO, et al. (2007) A continuous, high-resolution 8500-yr snow-avalanche record from western Norway. *Holocene* 17: 269–277.

Nesje A, Dahl SO, Thun T et al. (2008) The 'Little Ice Age' glacial expansion in western Scandinavia: Summer temperature or winter precipitation? *Climate Dynamics* 30: 789–801.

Nesje A, Kvamme M and Rye N (1989) Neoglacial gelifluction in the Jostedalsbreen region, Western Norway: Evidence from dated buried palaeopodsols. *Earth Surface Processes and Landforms* 14: 259–270.

Nesje A and Matthews JA (2024) Holocene glacial landscapes of the Scandinavian peninsula. In: Palacios D, Hughes PD, Jomelli V et al. (eds) *European Glacial Landscapes: The Holocene*. Amsterdam: Elsevier, pp.245–274.

Nicholson DT (2009) Holocene microweathering rates and processes on ice-eroded bedrock, Røldal area, Hardangervidda, Southern Norway. In: Knight J and Harrison S (eds) *Periglacial and Paraglacial Processes and Environments*, vol. 320. London: Geological Society, pp.29–49, Special Publications.

Norges geologiske undersøkelse (2025) 'Løsmasser'. Available at: https://geo.ngu.no/kart/losmasse_mobil/ (accessed 12 December 2024).

Oldfield F (1977) Lakes and their drainage basins as units of sediment-based ecological study. *Progress in Physical Geography* 1: 460–504.

Olsen T, Borella J and Stahl T (2020) Clast transport history influences Schmidt hammer rebound values. *Earth Surface Processes and Landforms* 45: 1392–1400.

Paus A and Haugland V (2017) Early- to mid-Holocene forestline and climate dynamics in Southern Scandes mountains inferred from contrasting megafossil and pollen data. *Holocene* 27: 361–383.

Phillips JD (2021) *Landscape Evolution: Landforms, Ecosystems and Soils*. Amsterdam: Elsevier.

Proceq (2017) *Concrete Test Hammer ("Original Schmidt"). Operating Instructions*. Schwerzenbach: Proceq.

Pytten M (2024) *Accuracy Assessment of the Schmidt Hammer Exposure-Age Dating Method and Comparative Analysis of Temporal Distributions of Large Rock Slope Failures in the Western Gneiss Region, Norway*. Master's Thesis: Norwegian University of Science and Technology (NTNU).

Regnéll C, Briner JP, Haflidason H et al. (2022) Deglaciation of the Scandinavian ice sheet and a Younger Dryas ice cap in the outer Hardangerfjorden area, Southwestern Norway. *Boreas* 51: 255–273.

Reynard E (2005) Géomorphosites et paysages. *Géomorphologie: Relief, Processus, Environment* 3: 181–188.

Reynard E, Coratza P and Regolini-Bissig G (eds)(2009) *Geomorphosites*. Munich: Verlag Dr. Friedrich Pfeil.

Roberts D (2003) The Scandinavian caledonides: Event chronology, palaeogeographic settings and likely modern analogues. *Tectonophysics* 365: 283–299.

Rode M and Kellerer-Pirklbauer A (2012) Schmidt-hammer exposure-age dating (SHD) of rock glaciers in the Schöderkogel-Eisenhut area, Schladminger Tauern Range, Austria. *Holocene* 22: 761–771.

Romundset A, Akçar N, Fredin O et al. (2023) Early Holocene thinning and final demise of the Scandinavian ice sheet across the main drainage divide of Southern Norway. *Quaternary Science Reviews* 317: 108274.

Santos-González J, González-Gutiérrez RB, Gómez-Villar A et al. (2024) Application of the Schmidt-hammer for relative-age dating of glacial and periglacial landforms in the Cantabrian mountains (NW Spain). *Geomorphology* 456: 109210.

Santos-González J, Palacios D, González-Gutiérrez R et al. (2026) Holocene glacial–paraglacial–periglacial transitions of a Sub-Arctic glacial cirque, Fremri-Grasárdalur, Northern Iceland *Permafrost and Periglacial Processes* 37: 78–106.

Scapozza C (2016) Evidence of paraglacial and paraperiglacial crisis in Alpine sediment transfer since the last glaciation (Ticino, Switzerland). *Quaternaire* 27: 139–155.

Scapozza C, Del Siro C, Lambiel C et al. (2021) Schmidt hammer exposure-age dating of periglacial and glacial landforms in the southern Swiss Alps based on R-value calibration using historical data. *Geographica Helvetica* 76: 401–423.

Scotti R, Brardinoni F, Crosta GB et al. (2017) Time constraints for post-LGM landscape response to deglaciation in Val Viola, Central Italian Alps. *Quaternary Science Reviews* 177: 10–33.

Sejrup HP and Hjelstuen BO (2022) The North Sea and mid-Norwegian continental margin. In: Palacios D, Hughes PD, García-Ruiz JM et al. (eds) *European Glacial Landscapes: Maximum Extent of Glaciations*. Amsterdam: Elsevier, pp.65–73.

Shakesby RA (1997) Pronival (protalus) ramparts: A review of forms, processes, diagnostic criteria and palaeoenvironmental implications. *Progress in Physical Geography* 21: 394–418.

Shakesby RA, Matthews JA and Owen G (2006) The Schmidt hammer as a relative-age dating tool and its potential for calibrated-age dating in Holocene glaciated environments. *Quaternary Science Reviews* 25: 2846–2867.

Shakesby RA, Matthews JA, Winkler S et al. (2020) Early-Holocene moraine chronology, Sognefjell area, Southern Norway: Evidence for multiple glacial and climatic fluctuations within the Erdalen event (~10.2–9.7 ka) *Norwegian Journal of Geology* 100: 202014.

Sollid JL and Kjenstad K (1980) Hovedflaten (Yngre Dryas' Havnivå) som basis for kvartær kronologi i Midt-Norge. Et metodeforsøk. *Norsk geografisk tidsskrift* 34: 93–96.

Statham I (1976) A scree slope rockfall model. *Earth Surface Processes* 1: 43–62.

Stokke J (1983) Kvartærgeologisk kartlegging med oppfølgende sand og grusundersøkelser i Norddal kommune, Møre og Romsdal. NGU Report 1560/30.

Støren EN, Dahl SO, Nesje A et al. (2010) Identifying the sedimentary imprint of high-frequency Holocene river floods in lake sediments: Development and application of a new method. *Quaternary Science Reviews* 29: 3021–3033.

Støren EN, Kolstad EW and Paasche Ø (2012) Linking past flood frequencies in Norway to regional atmospheric circulation anomalies. *Journal of Quaternary Science* 27: 71–80.

Stroeven AP, Hättestrand C, Kleman J et al. (2016) Deglaciation of Fennoscandia. *Quaternary Science Reviews* 147: 91–121.

Sumner P and Nel W (2002) The effect of rock moisture on Schmidt hammer rebound: Tests on rock samples from Marion Island and South Africa. *Earth Surface Processes and Landforms* 27: 1137–1142.

Svendsen JI and Mangerud J (1987) Late Weichselian and Holocene sea-level history for a cross-section of Western Norway. *Journal of Quaternary Science* 2: 113–132.

Tennøy PM and Askheim S (2025) Trollstigen. Store Norske Leksikon. Available at: https://snl.no.Trollstigen (accessed 21 September 2025).

Toebes C and Ouryvaev V (eds)(1970) *Representative and Experimental Basins: An International Guide for Research and Practice*. Paris: UNESCO.

Tomkins MD, Dortch JM and Hughes PD (2016) Schmidt hammer exposure dating (SHED): Establishment and implications for the retreat of the last British ice sheet. *Quaternary Geochronology* 33: 46–60.

Tomkins MD, Dortch JM, Hughes PD et al. (2018) Rapid age assessment of glacial landforms in the Pyrenees using Schmidt hammer exposure dating (SHED). *Quaternary Research* 90: 26–37.

Tonkin TN (2023) The paraglacial adjustment of an Alpine lateral moraine, Bas Glacier d'Arolla, Switzerland. *Physical Geography* 44: 643–659.

Tveten E, Lutro O and Thorsnes T (1998) *Geologisk kart over Noreg, bergrunnskart Ålesund, M 1:125,000*. Trondheim: Norges Geologiske Undersøkelse.

Vasskog K, Nesje A, Støren EN et al. (2011) A Holocene record of snow-avalanche and flood activity reconstructed from a lacustrine sedimentary sequence in Oldevatnet, Western Norway. *Holocene* 21: 597–614.

Walk J (2026) Expanding the Late Quaternary morphochronology of Atacama's coastal alluvial fans by Schmidt hammer exposure dating reveals spatially distinct genesis. *Quaternary Science Advances* 21: 100305.

Wanner H, Beer J, Bütikofer J et al. (2008) Mid- to Late-Holocene climate change: An overview. *Quaternary Science Reviews* 27: 1791–1828.

Wilson P, Dunlop P, Millar C et al. (2019a) Age determination of glacially-transported boulders in Ireland and Scotland using Schmidt-hammer exposure-age dating (SHD) and terrestrial cosmogenic nuclide (TCN) exposure-age dating. *Quaternary Research* 92: 570–582.

Wilson P, Linge H, Matthews JA et al. (2019b) Comparative numerical surface exposure-age dating (^{10}Be and Schmidt hammer) of an Early-Holocene rock avalanche at Alstadfjellet, Valldalen, Southern Norway. *Geografiska Annaler Series A* 101: 293–309.

Wilson P and Matthews JA (2016) Age assessment and implications of Late Quaternary periglacial and paraglacial landforms on Muckish mountain, Northwest Ireland, based on Schmidt-Hammer exposure-age dating (SHD). *Geomorphology* 270: 134–144.

Wilson P, Matthews JA, Mourne RW et al. (2020) Interpretation, age and significance of a relict paraglacial and periglacial boulder-dominated landform assemblage in Alnesdalen, Romsdal-salpane, Southern Norway. *Geomorphology* 369: 107362.

Winkler S (2009) First attempt to combine terrestrial cosmogenic nuclide (^{10}Be) and Schmidt hammer relative-age dating: Strauchon Glacier, Southern Alps, New Zealand. *Central European Journal of Geosciences* 1: 274–290.

Winkler S (2025) Improved chronological constraints for Holocene rock glacier activity in the Ben Ohau range, Southern Alps/New Zealand. *Holocene* 35: 352–372.

Winkler S and Lambiel C (2018) Age constraints of rock glaciers in the Southern Alps/New Zealand – Exploring their palaeoclimatic potential. *Holocene* 28: 778–790.

Winkler S, Matthews JA, Haselberger S et al. (2020) Schmidt-hammer exposure-age dating (SHD) of sorted stripes on Juvflye, Jotunheimen (Central South Norway): Morphodynamic and palaeoclimatic implications. *Geomorphology* 353: 107014.

Winkler S, Matthews JA, Mourne RW et al. (2016) Schmidt-hammer exposure ages from periglacial patterned ground (sorted circles) in Jotunheimen, Norway, and their interpretative problems. *Geografiska Annaler, Series A* 98: 265–285.